



This is to certify that the

dissertation entitled

In-situ straining of Cu-10Ni-6Sn spinodal alloy

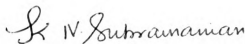
in High Voltage Electron Microscope

presented by

Tong-Chang Lee

has been accepted towards fulfillment  
of the requirements for

Ph. D. degree in Materials Science



Major professor

Date 10/17/85



RETURNING MATERIALS:  
Place in book drop to  
remove this checkout from  
your record. FINES will  
be charged if book is  
returned after the date  
stamped below.

JUN 27 8 2001

**IN-SITU STRAINING OF Cu-10Ni-6Sn SPINODAL ALLOYS  
IN HIGH VOLTAGE ELECTRON MICROSCOPE**

**By  
Tong-Chang Lee**

**A THESIS**

**Submitted to  
Michigan State University  
in partial fulfillment of the requirements  
for the degree of**

**DOCTOR OF PHILOSOPHY**

**Department of Metallurgy, Mechanics and Materials Science**

**1985**



## ABSTRACT

### IN-SITU STRAINING OF Cu-10Ni-6Sn SPINODAL ALLOYS IN HIGH VOLTAGE ELECTRON MICROSCOPE

By

Tong-Chang Lee

In-situ straining of homogeneous as well as spinodally modulated specimens of Cu-10Ni-6Sn alloy was carried out in the High Voltage Electron Microscope. Dislocations were observed to reorient themselves in a continuous fashion during their motion. Dislocation motion was found to be smooth in homogeneous specimens, whereas it was discontinuous in specimens with modulated structure. Video recording of dynamic dislocation events during straining and Burgers vector analysis of these dislocations, in their relaxed configuration under stress were carried out. Such analyses indicated that these dislocations existed in screw orientation in homogenized specimens and in specimens that have undergone early stages of decomposition. However, extensive modulation due to longer aging causes these dislocations to possess a mixed character having Burgers vector at about  $60^\circ$  to their line direction.

Tong-Chang Lee

A discussion of current theories on age-hardening in spinodal alloys is presented. Correlation of the experimental observations with these theories is provided.

## ACKNOWLEDGEMENTS

The author would like to thank his advisor, Professor K. N. Subramanian for his help and support over the course of this investigation. Special thanks are given to Professor Masaharu Kato of the Tokyo Institute of Technology for his guidance and encouragement in the first two years of the author's graduate career. Special thanks are also due to Professor K. Mukherjee, Professor N. Altiero of the Department of Metallurgy, Mechanics and Materials Science, and Professor J. Bass of the Department of Physics for their helpful discussions and encouragement. The author would also like to thank Shekhar Subramoney, a research partner and a friend, for his generous help and friendship over the past four years.

The author would also like to acknowledge the support of the Department of Energy through contract DE-AC02-81ER10924 and DE-FG02-84ER45060, and through their support of the HVEM center at Argonne National Laboratories. Special thanks are due to Mr. E. Ryan and Mr. A. Phillippedes for their assistance at the Argonne HVEM facility. Special thanks are also due to Professor Karen Baker and the staff of the Center of Electron Optics at Michigan State University for providing the use of the electron microscopy facilities for the experiments.

## TABLE OF CONTENTS

	Page
LIST OF TABLES .....	iv
LIST OF FIGURES .....	v
Chapter	
1 INTRODUCTION .....	1
2 THEORIES OF AGE-HARDENING BY SPINODAL DECOMPOSITION .....	10
2.1 Theory by Cahn .....	10
2.2 Theory by Dahlgren .....	18
2.3 Theory by Carpenter .....	19
2.4 Theory by Ghista and Nix .....	20
2.5 Theory by Ditchek and Schwartz .....	22
2.6 Theory by Hanai et al. ....	23
2.7 Theory by Kato, Mori and Schwartz (K-M-S Theory) .....	24
2.8 Theory by Ardell .....	28
3 EXPERIMENTAL PROCEDURE .....	32
3.1 Specimen Preparation .....	32
3.2 <u>In-situ</u> Deformation in HVEM .....	40
4 EXPERIMENTAL RESULTS .....	47
4.1 General Observations .....	47
4.2 Character Analyses of Dislocations that were Mobile during <u>In-situ</u> Straining .....	68
4.2.1 As-quenched specimens .....	69
4.2.2 Specimens aged for 20 minutes .....	80
4.2.3 Specimens aged for 40 minutes .....	90
4.2.4 Specimens aged for 60 minutes .....	98
5 DISCUSSION .....	112
5.1 Theoretical Models .....	112
5.2 <u>In-situ</u> Deformation in HVEM .....	126
6 CONCLUSIONS .....	138
REFERENCES .....	141

## LIST OF TABLES

Table	Page
1    Chemical thinning and electropolishing data for the preparation of specimens for <u>in-situ</u> straining. ....	35
2    Summary of the dislocation character analyses of thin foil specimens deformed <u>in-situ</u> . ....	111
3    Comparison of the experimental and theoretically predicted values of incremental yield stress of Cu-Ni-Fe alloys. Theoretical values are obtained by using equations derived by Ardell, Cahn, and Kato et al. [11]. ....	113
4    Values of the parameters used in estimating the incremental yield stress in Cu-Ni-Fe alloys [11]. $\Gamma$ was calculated from Equation (44) using $\ln(L/r) = 4$ . ....	114
5    Values of the parameters used in estimating the incremental yield stress decomposition in a Cu-10Ni-6Sn alloy aged at 623 K for various lengths of time (in minutes) [45]. ....	116
6    Comparison of the experimental and theoretically predicted values of incremental yield stress of Cu-10Ni-6Sn spinodal alloy aged for various length of time at 623 K. ....	117
7    Comparison of numerically calculated values of amplitude, $v$ , and maximum slope, $\theta_e$ , for edge dislocations in Cu-33.5Ni-15.0Fe alloy and values predicted by Cahn's model [3]. ....	122

## LIST OF FIGURES

Figure	Page
1	(a) The free energy versus composition curve for a binary alloy at temperature $T_0$ . (b) Phase diagram with miscibility gap, chemical spinodal and coherent spinodal for the binary alloy in (a) [1]. ..... 3
2	Schematic representation of Equation (15) of the force field on the dislocations [3]. ..... 15
3	Schematic representation of the force field on mixed dislocations [10]. ..... 26
4	Illustration of the basic geometry of Mott statistics [43]. " $L_m$ " is the Mott's spacing, " $v$ " is the range of interaction between an obstacle and a dislocation, and " $h/2$ " is the amplitude of the zig-zag dislocation configuration. .... 30
5	Thermal and mechanical treatment flow chart for specimen preparation. .... 33
6	Schematic representation of electropolishing steps in preparation of specimens for <u>in-situ</u> straining in HVEM. .... 34
7	Schematic of the electropolishing unit for jet polishing. .... 38
8	Schematic of the electropolishing unit for final polishing. .... 39
9	(a) The Gatan double-tilt microtensile stage for <u>in-situ</u> straining in HVEM. (b) Photograph of a specimen mounted on the microtensile stage. .... 41
10	The deformation rate versus applied voltage curve of the Gatan microtensile stage. .... 42

11	Radiation damage in a specimen examined at 1 MeV over a time period of 12 minutes (a) t = 0 minute, (b) t = 1 minute, (c) t = 3 minutes, (d) t = 12 minutes. ....	43
12	Series of micrographs showing motion of dislocations along slip traces in homogenized specimen during <u>in-situ</u> deformation in HVEM. ....	49
13	Series of micrographs showing motion of dislocations along slip traces in homogenized specimen during <u>in-situ</u> deformation in HVEM. ....	50
14	Series of micrographs showing motion of dislocations along slip traces in homogenized specimen during <u>in-situ</u> deformation in HVEM. ....	51
15	Series of micrographs showing motion of dislocations along slip traces in homogenized specimen during <u>in-situ</u> deformation in HVEM. ....	53
16	Series of micrographs showing motion of dislocations along slip traces in an aged specimen during <u>in-situ</u> deformation in HVEM. Specimen aged at 623 K for 20 minutes. ....	54
17	Series of micrographs showing motion of dislocations along slip traces in an aged specimen during <u>in-situ</u> deformation in HVEM. Specimen aged at 623 K for 20 minutes. ....	55
18	Series of micrographs showing motion of dislocations along slip traces in an aged specimen during <u>in-situ</u> deformation in HVEM. Specimen aged at 623 K for 20 minutes. ....	56
19	Series of micrographs showing motion of dislocations along slip traces in an aged specimen during <u>in-situ</u> deformation in HVEM. Specimen aged at 623 K for 20 minutes. ....	57
20	Series of micrographs showing motion of dislocations along slip traces in an aged specimen during <u>in-situ</u> deformation in HVEM. Specimen aged at 623 K for 40 minutes. ....	59

21	Series of micrographs showing motion of dislocations along slip traces in an aged specimen during <u>in-situ</u> deformation in HVEM. Specimen aged at 623 K for 40 minutes. ....	60
22	Series of micrographs showing motion of dislocations along slip traces in an aged specimen during <u>in-situ</u> deformation in HVEM. Specimen aged at 623 K for 60 minutes. ....	62
23	Series of micrographs showing motion of dislocations along slip traces in an aged specimen during <u>in-situ</u> deformation in HVEM. Specimen aged at 623 K for 60 minutes. ....	63
24	Series of micrographs showing motion of dislocations along slip traces in an aged specimen during <u>in-situ</u> deformation in HVEM. Specimen aged at 623 K for 60 minutes. ....	64
25	Typical features of an opening crack in a specimen during <u>in-situ</u> deformation in HVEM. ....	66
26	Schematic representation of (a) the parallelogram-shaped voids ahead of an opening crack, and (b) the arrangement of the dislocations near the shearing edges producing parallelogram-shaped voids. ....	67
27	Burgers vector analysis of dislocations in slip trace A and B of a homogenized specimen during <u>in-situ</u> straining in HVEM. (a) $\vec{g} = [2\bar{2}0]$ (b) $\vec{g} = [\bar{1}1\bar{1}]$ (c) $\vec{g} = [00\bar{2}]$ ....	70
28	Burgers vector analysis of dislocations in slip trace C and D of a homogenized specimen during <u>in-situ</u> straining in HVEM. (a) $\vec{g} = [\bar{1}1\bar{1}]$ (b) $\vec{g} = [\bar{2}20]$ (c) $\vec{g} = [\bar{1}11]$ (d) $\vec{g} = [00\bar{2}]$ ....	72
29	Burgers vector analysis of dislocations in slip trace E and F of a homogenized specimen during <u>in-situ</u> straining in HVEM. (a) $\vec{g} = [\bar{1}11]$ (b) $\vec{g} = [002]$ (c) $\vec{g} = [\bar{1}1\bar{1}]$ ....	75
30	Burgers vector analysis of dislocations in slip trace G of a homogenized specimen during <u>in-situ</u> straining in HVEM. (a) $\vec{g} = [\bar{1}1\bar{1}]$ (b) $\vec{g} = [\bar{1}11]$ ....	77



- 31 Burgers vector analysis of dislocations in slip trace H of a homogenized specimen during in-situ straining in HVEM.  
(a)  $\vec{g} = [1\bar{1}1]$  (b)  $\vec{g} = [\bar{1}11]$  ..... 79
- 32 Burgers vector analysis of dislocations in slip trace I and J of an aged specimen during in-situ straining in HVEM.  
Specimen aged at 623 K for 20 minutes.  
(a)  $\vec{g} = [200]$  (b)  $\vec{g} = [2\bar{2}0]$   
(c)  $\vec{g} = [0\bar{2}0]$  (d)  $\vec{g} = [\bar{2}20]$  ..... 81
- 33 Burgers vector analysis of dislocations in slip trace K and L of an aged specimen during in-situ straining in HVEM.  
Specimen aged at 623 K for 20 minutes.  
(a)  $\vec{g} = [\bar{1}1\bar{1}]$  (b)  $\vec{g} = [00\bar{2}]$   
(c)  $\vec{g} = [2\bar{2}0]$  (d)  $\vec{g} = [\bar{1}11]$  ..... 84
- 34 Burgers vector analysis of dislocations in slip trace M and N of an aged specimen during in-situ straining in HVEM.  
Specimen aged at 623 K for 20 minutes.  
(a)  $\vec{g} = [\bar{1}3\bar{1}]$  (b)  $\vec{g} = [\bar{1}\bar{3}1]$   
(c)  $\vec{g} = [\bar{2}00]$  (d)  $\vec{g} = [1\bar{1}\bar{1}]$  ..... 86
- 35 Burgers vector analysis of dislocations in slip trace O of an aged specimen during in-situ straining in HVEM.  
Specimen aged at 623 K for 20 minutes.  
(a)  $\vec{g} = [\bar{1}11]$  (b)  $\vec{g} = [2\bar{2}0]$   
(c)  $\vec{g} = [1\bar{1}1]$  (d)  $\vec{g} = [\bar{1}1\bar{3}]$  ..... 88
- 36 Burgers vector analysis of dislocations in slip trace P of an aged specimen during in-situ straining in HVEM.  
Specimen aged at 623 K for 40 minutes.  
(a)  $\vec{g} = [1\bar{1}1]$  (b)  $\vec{g} = [\bar{1}11]$  ..... 91
- 37 Burgers vector analysis of dislocations in slip trace Q of an aged specimen during in-situ straining in HVEM.  
Specimen aged at 623 K for 40 minutes.  
(a)  $\vec{g} = [\bar{2}20]$  (b)  $\vec{g} = [1\bar{1}\bar{3}]$  (c)  $\vec{g} = [1\bar{1}1]$  ..... 93
- 38 Burgers vector analysis of dislocations in slip trace R of an aged specimen during in-situ straining in HVEM.  
Specimen aged at 623 K for 40 minutes.  
(a)  $\vec{g} = [\bar{2}20]$  (b)  $\vec{g} = [1\bar{1}\bar{1}]$  (c)  $\vec{g} = [\bar{1}1\bar{1}]$  ..... 95

- 39 Burgers vector analysis of dislocations in slip trace S of an aged specimen during in-situ straining in HVEM.  
Specimen aged at 623 K for 40 minutes.  
(a)  $\vec{g} = [\bar{1}1\bar{1}]$  (b)  $\vec{g} = [\bar{2}20]$  (c)  $\vec{g} = [00\bar{2}]$  ..... 97
- 40 Burgers vector analysis of dislocations in slip trace T of an aged specimen during in-situ straining in HVEM.  
Specimen aged at 623 K for 60 minutes.  
(a)  $\vec{g} = [\bar{1}1\bar{1}]$  (b)  $\vec{g} = [00\bar{2}]$   
(c)  $\vec{g} = [\bar{2}20]$  (d)  $\vec{g} = [\bar{1}\bar{1}1]$  ..... 99
- 41 Burgers vector analysis of dislocations in slip trace U of an aged specimen during in-situ straining in HVEM.  
Specimen aged at 623 K for 60 minutes.  
(a)  $\vec{g} = [\bar{1}1\bar{1}]$  (b)  $\vec{g} = [\bar{1}\bar{1}1]$  (c)  $\vec{g} = [00\bar{2}]$  ..... 101
- 42 Burgers vector analysis of dislocations in slip trace V of an aged specimen during in-situ straining in HVEM.  
Specimen aged at 623 K for 60 minutes.  
(a)  $\vec{g} = [\bar{1}1\bar{1}]$  (b)  $\vec{g} = [\bar{1}\bar{1}1]$  (c)  $\vec{g} = [00\bar{2}]$  ..... 103
- 43 Burgers vector analysis of dislocations in slip trace W of an aged specimen during in-situ straining in HVEM.  
Specimen aged at 623 K for 60 minutes.  
(a)  $\vec{g} = [\bar{1}1\bar{1}]$  (b)  $\vec{g} = [\bar{1}\bar{1}1]$  (c)  $\vec{g} = [00\bar{2}]$  ..... 105
- 44 Burgers vector analysis of dislocations in slip trace X of an aged specimen during in-situ straining in HVEM.  
Specimen aged at 623 K for 60 minutes.  
(a)  $\vec{g} = [\bar{1}1\bar{1}]$  (b)  $\vec{g} = [\bar{2}0\bar{2}]$   
(c)  $\vec{g} = [\bar{2}20]$  (d)  $\vec{g} = [0\bar{2}\bar{2}]$  ..... 107
- 45 Burgers vector analysis of dislocations that lie along directions marked Y and Z in an aged specimen during in-situ straining in HVEM.  
Specimen aged at 623 K for 60 minutes.  
(a)  $\vec{g} = [\bar{1}1\bar{1}]$  (b)  $\vec{g} = [00\bar{2}]$  (c)  $\vec{g} = [\bar{1}\bar{1}1]$  ..... 109

## CHAPTER 1

### INTRODUCTION

In recent years, a new class of materials, the spinodal alloys [1, 2], which exhibit some unusual properties, have generated considerable interest in the field of materials science and engineering. The interests in these materials are due to their excellent properties such as mechanical, magnetic, electrical, etc. More importantly, the enhancement of these properties are a direct consequence of their microstructure, which is produced by a solid-solid phase transformation known as spinodal decomposition. A large number of theoretical models have been proposed to explain the age-hardening effect [2 - 11], i.e., the increase in yield stress due to aging, in these alloys. In some of the proposed theories, the character of mobile dislocation plays a very important role in determining the incremental yield stress due to spinodal decomposition. In this study, the main emphasis is placed on 1) study of the mobile dislocation behavior in a spinodally modulated structure during in-situ straining in High Voltage Electron

Microscope (HVEM), 2) experimental determination of the character of dislocations which are responsible for the plastic deformation by using in-situ deformation techniques in HVEM, and 3) correlation between the theoretical models and the experimental results.

The concept of spinodal decomposition was first described by Gibbs in 1877 [12] as a limit of metastability for fluid phases, and by 1890 such a transformation had been termed as spinodal decomposition [13]. In order to understand why the spinodal marks the limit of metastability, let us consider a binary alloy system in which the Helmholtz free energy,  $F$ , varies with composition at a temperature  $T$ , as shown in Figure 1(a). There are two inflection points,  $C_{s1}$  and  $C_{s2}$ , defined by

$$(\partial^2 F / \partial C^2)_{T,V} = F'' = 0, \quad (1)$$

where  $C$  is the atomic fraction of the secondary component and  $V$  is the volume of the material.  $C_{s1}$  and  $C_{s2}$ , on the other hand, are points of common tangency to this curve and they define the composition of the coexisting phases at  $T$ . The locus of points satisfying Equation (1) for different temperatures is called the spinodal (chemical spinodal) and is shown by the dashed curve in Figure 1(b). The solid line in the same figure, the miscibility gap, represents the locus of points  $C_{s1}$  and  $C_{s2}$  for different temperatures. For

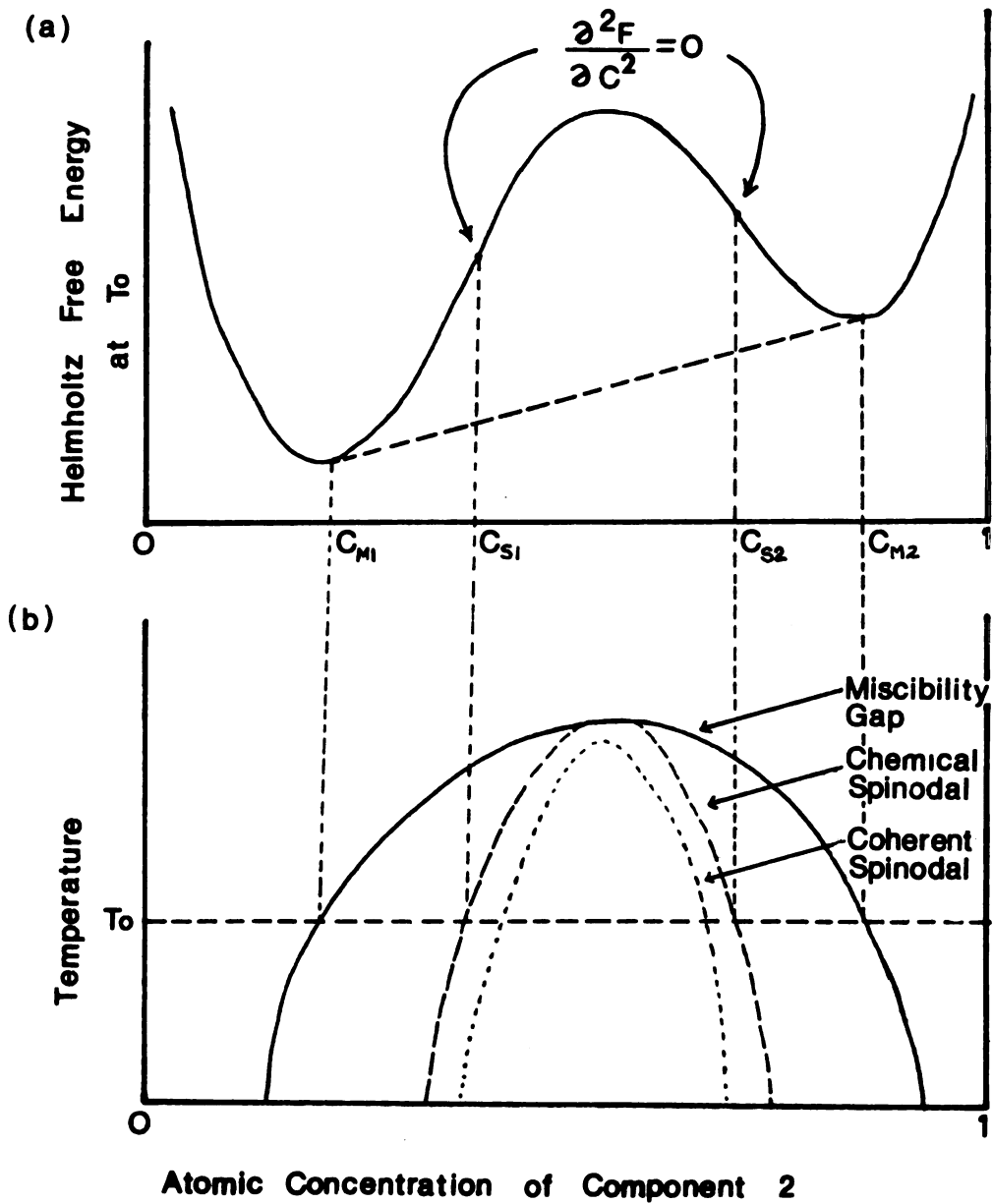


**Figure 1** (a) The free energy versus composition curve for a binary alloy at temperature  $T_0$ .  
 (b) Phase diagram with miscibility gap, chemical spinodal and coherent spinodal for the binary alloy in (a) [1].

a homogeneous phase with a concentration outside the spinodal at temperature  $T_0$ ,  $F''$  is positive, and small fluctuations in composition raises the free energy. Therefore, this phase is considered to be a metastable phase. However, for a homogeneous phase with a concentration inside the spinodal,  $F''$  becomes negative, and small fluctuations in composition always lowers its free energy since this phase is unstable. Such fluctuations should spontaneously be enhanced until the lowest free energy is achieved when a two-phase mixture with two phases given by the two common tangents is formed. Therefore, the spinodal line can be defined as the boundary between unstable and metastable phases.

The first experimental observation of spinodal decomposition was made in early 1940's. At that time, Bradley [1] reported observation of sidebands around the sharp Bragg spots of the x-ray diffraction pattern from a Cu-Ni-Fe alloy that had been quenched and then aged inside the miscibility gap. Further observations on the same alloy were also made by Daniel and Lipson [14, 15], who concluded that the sidebands could be explained by a periodic modulation of composition in the  $\langle 100 \rangle$  directions. From the spacing of the sidebands, they were able to determine the wavelength of the modulation, which was of the order of 100  $\text{\AA}$ .

The first explanation of the periodicity of composition was given by Hillert [16, 17]. Since there is no thermodynamic barrier inside the spinodal, the decomposition is determined solely by diffusion. Hillert derived a flux equation for one-dimensional diffusion on a discrete lattice. This equation differed from the usual classical diffusion equation by including one more term that allowed for the effect of the driving force due to the interfacial energy between adjacent atomic planes that differed in composition. Hillert solved this flux equation numerically, and found that inside the spinodal it yielded a periodic variation of composition with distance. Furthermore, the wavelength of the modulation was of the same order as that observed in the Cu-Ni-Fe alloy [18].

Cahn [19, 20] modified Equation (1) by adding an additional term to accommodate the effect of coherency strains. According to him

$$F'' + 2\eta''Y = 0, \quad (2)$$

where " $\eta$ " is defined by  $\partial \ln a / \partial c$  with " $a$ " as the lattice parameter and " $c$ " as the concentration of the secondary element, and " $Y$ ", for the case of the  $\langle 100 \rangle$  modulation, can be expressed in terms of the elastic constants  $C_{ij}$ , as

$$Y = \frac{(C_{11} - C_{12})(C_{11} + 2C_{12})}{C_{11}}. \quad (3)$$

The locus of points satisfying equation (2), which always lies inside the chemical spinodal, is defined as the coherent spinodal and is shown in Figure 1(b).

These are some of the general concepts of spinodal decomposition. Detailed discussions on spinodal decomposition by Hilliard [1], Hoffman [21], Cahn [22], Ditchek and Schwartz [2], and Soffa and Laughlin [23] are available in published literature.

Experimental studies on the mechanical properties of spinodal alloys have been carried out by various investigators [5, 6, 24 - 40]. In an extensive study on the Cu-Ni-Fe alloys was carried out by Butler and Thomas [24], the wavelength of modulation,  $\lambda$ , was determined from the sidebands of TEM diffraction patterns and the amplitude of the decomposition,  $A$ , was determined from the magnetic Curie point measurements. Their results indicated that the incremental yield stress increased linearly with  $A$  and was independent of  $\lambda$ . Dahlgren's studies [5] on the same alloy system concurred with this observation.

Carpenter [6] investigated the mechanical properties of polycrystalline Au-Pt alloys. The wavelength of the composition modulation was calculated from the x-ray sidebands. He found that the presence of spinodal



decomposition caused a significant increase in work-hardening rate and the incremental yield stress. Carpenter also observed that the specimens became brittle with increased extent of spinodal decomposition. He has attributed this behavior to grain boundary precipitates. Such loss of ductility and intergranular fracture have also been observed by Douglass and Barbee [25] in Al-Zn alloy.

In the investigation on the mechanical properties of Cu-Ni-Cr alloy, Wu and Thomas [26] found that the yield stress increased with the extent of decomposition. A drop in yield stress after aging at 700°C for 166 hours was observed, and this was attributed to the loss of coherency of the particles. Their results also indicated that there is a dependence of the increment of yield stress on  $\Delta a$ , the variation of lattice parameter. Chou et al. [27] have pointed out that the mechanical strengthening in Cu-Ni-Cr alloy can be analyzed in terms of the interaction of dislocations with the internal stress field associated with the spinodal decomposition.

Greggi and Soffa [28, 29] studied the strengthening of Cu-Ti single crystals aged at 678 K. Their results showed that the aging response was weak for the first 10 minutes of aging but increased significantly between 10 and 1000 minutes. The rate of strengthening decreased sharply at this point, but the yield strength continued to rise slowly

with increased aging time. Their findings indicated that the strengthening behavior is derived mainly from the coherency strain caused by spinodal decomposition and a minor contribution from order hardening. Investigations on the age-hardening in Cu-Ti alloys were also carried out by Wagner [30], Laughlin and Cahn [31], Kratochvil and Haasen [32], and Datta and Soffa [33].

Kato and Schwartz [34] found that the increase in yield stress due to spinodal decomposition is temperature independent in Cu-10Ni-6Sn alloy. The activation volume measured by the strain-rate change test revealed no marked difference between aged and homogenized specimens. The work-hardening rate was almost independent of the heat-treatment of the alloy. These results have been verified and extended to cover a wider range of temperature and extents of decomposition by Vilassakdanont and Subramanian [35], and Lee et al. [36]. They have also found that the percentage elongation to fracture is independent of the extent of aging. Louzon [37], and Schwartz and Pleves [38] have also studied the mechanical properties of Cu-Ni-Sn alloys.

Quin and Schwartz [39] have investigated the fatigue properties of the Cu-Ni-Sn alloy that have undergone early stages of decomposition. Their results showed only modest improvement in the apparent fatigue limit while tensile

yield strength is increased by a factor of 2.5 in specimens aged for 15 minutes at 390°C. Their conclusion attributed this cyclic softening phenomenon to the mechanism of localized demodulation of the spinodal microstructure by the to and fro motion of dislocations. Similar results were also noted by Sinning and Haasen [40] during their fatigue studies on Cu-4Ti single crystals.

## CHAPTER 2

### THEORIES OF AGE-HARDENING BY SPINODAL DECOMPOSITION

Various theories [2 - 11] have been proposed to explain the age-hardening mechanism by spinodal decomposition. In this chapter, a literature survey of various proposed theories is presented and their possible drawbacks are pointed out. Detailed comparison and modification on some of the theories, in order to find out the most suitable one for explaining the age-hardening mechanism in spinodal decomposition, are presented in Chapter 5.

#### 2.1 Theory by Cahn

This is one of the earliest theories that has been proposed to explain the mechanism of age-hardening by spinodal decomposition. In Cahn's model [3], the composition modulation in a spinodally decomposed alloy was described as the sum of three perpendicular  $\{100\}$  plane waves. By considering only a single Fourier component of the plane wave, the composition fluctuation " $\Delta c$ " along  $[001]$

direction in a cubic alloy can be represented in cartesian (x, y, z) coordinate system as

$$\Delta c = c - c_0 = A(\beta) \cos(\beta z), \quad (4)$$

where "c" and "c<sub>0</sub>" are the local and average composition of the alloy, "β" is the wave vector in the [001] direction (z-direction) and A(β) is the amplitude of composition modulation. The internal stress produced by this composition modulation is

$$\begin{aligned} \sigma_{xx} &= \sigma_{yy} = (\nabla \Delta c Y) = A \nabla Y \cos(\beta z), \\ \sigma_{zz} &= \sigma_{xy} = \sigma_{yz} = \sigma_{zx} = 0, \end{aligned} \quad (5)$$

where "∇" is the composition variation of the stress free lattice parameter "a", and "Y" has the same meaning as defined in Chapter 1. By superpositioning all the Fourier components whose wave vectors are in the [001] direction,

$$\begin{aligned} \sigma_{xx} &= \sigma_{yy} = S_2(z), \\ \sigma_{zz} &= \sigma_{xy} = \sigma_{yz} = \sigma_{zx} = 0, \end{aligned} \quad (6)$$

where S<sub>2</sub>(z) is obtained by integrating equation (5) over all Fourier components in the z-direction

$$S_2(z) = \nabla Y \int A(\beta) e^{-i\beta z} d\beta. \quad (7)$$

In a similar manner,  $S_1(x)$  and  $S_2(y)$ , for the [100] and [010] components respectively can be defined. Thus the interal stress resulting from all its Fourier components is

$$\sigma_s = \begin{pmatrix} S_2(y)+S_3(z) & 0 & 0 \\ 0 & S_1(x)+S_3(z) & 0 \\ 0 & 0 & S_1(x)+S_2(y) \end{pmatrix}. \quad (8)$$

For the particular case of the three perpendicular waves of the same wavelength  $\lambda$  ( $=2\pi/\beta$ ), as in the earlier stages of decomposition,  $S_1(x)$ ,  $S_2(y)$  and  $S_3(z)$  can be represented in a much simpler form,

$$\begin{aligned} S_1(x) &= A\eta Y \cos(\beta x), \\ S_2(y) &= A\eta Y \cos(\beta y), \text{ and} \\ S_3(z) &= A\eta Y \cos(\beta z). \end{aligned} \quad (9)$$

The force,  $\vec{F}$ , acting on a dislocation per unit length produced by a stress field,  $g$ , can be represented as

$$\vec{F} = (\vec{b} \cdot g) \times \vec{\xi}, \quad (10)$$

where  $\vec{b}$  is the Burgers vector and  $\vec{\xi}$  is the unit tangent line to the dislocation line. The glide component  $\vec{F}_g$  of the force in Equation (10) is given by

$$\vec{F}_g = (\vec{n} \times \vec{\xi}) (\vec{b} \cdot g \cdot \vec{n}), \quad (11)$$

wh

(8

Bu

on

n,

re

vi

p

d

a

R

t

c

c

where  $\vec{n}$  is the normal to the glide plane. Using Equations (8) and (11), the forces acting on a dislocation whose Burgers vector has components  $(b_1, b_2, b_3)$ , and is mobile on a glide plane whose unit normal has components  $(n_1, n_2, n_3)$ , can be written as

$$F_i = -(n_1 b_1 S_1 + n_2 b_2 S_2 + n_3 b_3 S_3). \quad (12)$$

For FCC spinodal alloys, the slip plane (111) can be represented as

$$x + y + z = \sqrt{3}d, \quad (13)$$

where "d" is the interplanar distance between the (111) planes. From Equation (12), the resolved force on a dislocation whose Burgers vector is parallel to the  $[1\bar{1}0]$  slip direction becomes

$$F_i = \frac{\sqrt{2}}{\sqrt{3}} (A\gamma b \sin[\frac{\theta(x+y)}{2}] \sin[\frac{\theta(x-y)}{2}]). \quad (14)$$

Rotating the coordinate system such that the x-axis is along the  $[110]$  direction and the y-axis is along the  $[1\bar{1}2]$  direction and combining with Equation (13), the force on a dislocation due to the internal stress field, as in Equation



(14), can be rewritten as

$$F_i = \frac{\sqrt{2}}{\sqrt{3}} [A\sigma Yb \sin(\frac{\theta x}{\sqrt{2}}) \sin(\frac{\theta y}{\sqrt{6}})]. \quad (15)$$

According to this equation, the force field on the (111) slip plane resembles a rectangular checkboard of alternating forces as shown in Figure 2. The sides of each one of these rectangles are the locus of zero force positions, and within each rectangle the "+" or "-" sign represents the maximum or minimum force which has an extremum in the center.

By using a string model for a mobile dislocation, Cahn obtained a force-balance equation for the forces acting on a dislocation line, present in its rest configuration, in the presence of the applied force field. This equation can be written as

$$\frac{\Gamma(\frac{d^2y}{dx^2})}{[1 + (\frac{dy}{dx})^2]^{3/2}} + \frac{\sqrt{2}}{\sqrt{3}} A\sigma Yb \sin(\frac{\theta x}{\sqrt{2}}) \sin(\frac{\theta y}{\sqrt{6}}) + \sigma b = 0. \quad (16)$$

In Equation (16), the first term is the force due to the curvature of the dislocation, where " $\Gamma$ " is the line tension of the dislocation, the second term is the force due to the internal stress field and the third term is the force due to the external applied stress whose resolved shear stress on

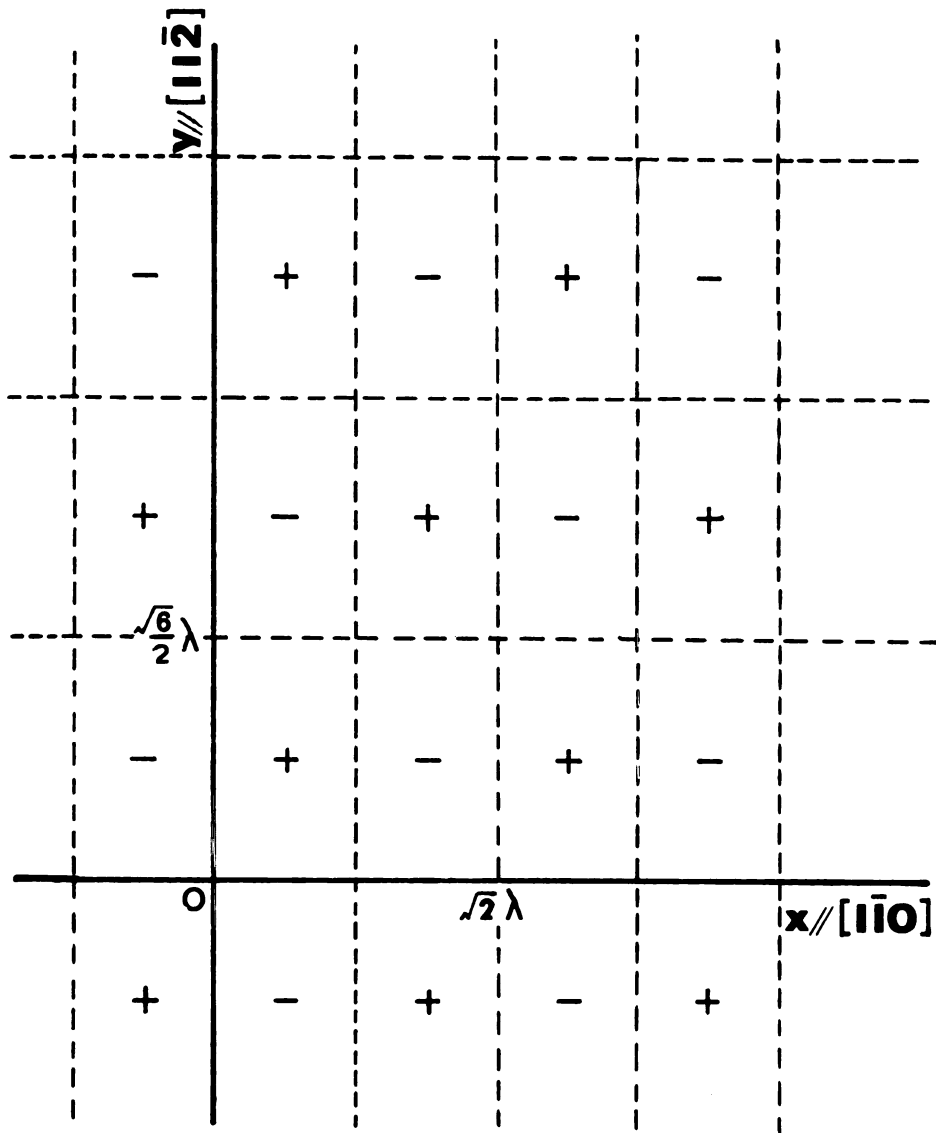


Figure 2 Schematic representation of Equation (15) of the force field on the dislocations [3].

the dislocation line is  $|\epsilon|$ . Equation (16) is known as the force-balance equation for a dislocation on the  $(111) [1\bar{1}0]$  slip system in an FCC spinodal structure.

By predicting that age-hardening in spinodal alloys is due to the motion of edge or screw dislocations, Cahn solved Equation (16) analytically by using an approximation method (Galerkin method). This was done by first assuming a sinusoidal form solution for the dislocation line

$$y = C_1 + C_2 \sin\left(\frac{\pi x}{\sqrt{2}}\right) \quad \text{for screw dislocations,} \quad (17)$$

and

$$x = B_1 + B_2 \sin\left(\frac{\pi y}{\sqrt{6}}\right) \quad \text{for edge dislocations.} \quad (18)$$

Using the Galerkin method, along with another assumption that  $\Delta\gamma b/\Gamma\delta \ll 1$ , the coefficients  $C_1$ ,  $C_2$ ,  $B_1$  and  $B_2$  were determined. For screw dislocations

$$\sin\left(\frac{\pi C_1}{\sqrt{6}}\right) = - \frac{\sqrt{3}\delta^2 \Gamma C_2}{2\sqrt{2}\Delta\gamma |b|} , \quad (19)$$

$$\cos\left(\frac{\pi C_1}{\sqrt{6}}\right) = - \frac{6\sigma}{\Delta\gamma C_2 \delta} , \quad (20)$$

$$C_2^2 = \frac{4}{3} \frac{\Delta^2 \gamma^2 b^2}{\delta^2 \Gamma^2} \left( 1 \pm 1 - \sqrt{\frac{54\sigma^2 \delta^2 \Gamma^2}{\Delta^2 \gamma^2 b^2}} \right) . \quad (21)$$

For edge dislocations

$$\sin\left(\frac{\theta B_1}{\sqrt{2}}\right) = - \frac{\sqrt{3}\theta^2 \Gamma B_1 |\sigma|}{6\sqrt{2} A \eta Y b}, \quad (22)$$

$$\cos\left(\frac{\theta B_1}{\sqrt{2}}\right) = - \frac{2\sqrt{3} |\sigma|}{A \eta Y B_1 \theta}, \quad (23)$$

$$B_1^2 = \frac{12 A^2 \eta^2 Y^2 b^2}{\theta^2 \Gamma^2} \left( 1 \pm 1 - \sqrt{\frac{\sigma^2 \Gamma^2 \theta^2}{A^2 \eta^2 Y^2 b^2}} \right). \quad (24)$$

The critical resolved shear stress (CRSS) is defined by the upper limit of the magnitude of the applied stress  $|\sigma|$  which would satisfy Equations (21) and (24). At applied stresses exceeding

$$|\sigma| = \frac{A^2 \eta^2 Y^2 b}{3\sqrt{6}\Gamma} \quad \text{for screw dislocations,} \quad (25)$$

or

$$|\sigma| = \frac{A^2 \eta^2 Y^2 b}{\sqrt{2} \theta \Gamma} \quad \text{for edge dislocations,} \quad (26)$$

no solution exists for Equation (16) and the dislocation should move continuously through the structure. Screw dislocations have a much smaller value of CRSS and hence are much easier to move than edge dislocations. Therefore, Cahn considered the motion of screw dislocations to be responsible for the age-hardening of spinodal alloys. From

Equations (25) and (26), it can also be seen that Cahn's theory predicts that the increase in yield stress will be proportional to  $A^2\lambda$ .

Unfortunately, Cahn's prediction of the incremental yield stress was proven to be too small compared with the experimental results. For example, according to Carpenter's study [6] of Au-Pt spinodal alloy, the observed incremental yield stress ( $\approx 70\text{MPa}$ ) was much larger than the one ( $\approx 5\text{MPa}$ ) predicted by Cahn's model. Similar disagreements have also been found by Douglass and Barbee [25], Ditchek and Schwartz [2], and Lefevre et al. [25]. Moreover, the  $A^2\lambda$  dependence of the incremental yield stress predicted by Cahn was also found to be inconsistent with experimental observations by Butler and Thomas [24], and Lefevre et al. [41]. In order to overcome the above mentioned disagreements between Cahn's theory and the experimental data, several other theoretical models have been proposed.

## 2.2 Theory by Dahlgren

Dahlgren obtained a theoretical expression for CRSS in FCC spinodal alloys as [4, 5]

$$\sigma = \frac{A\gamma}{3\sqrt{6}} \quad (27)$$

Equation (27) was derived by considering the coherency internal stress due to composition modulation, and its interaction with a glide dislocation. In general, Equation (27) is in better agreement with experimental data [2]. For Au-Pt system, Equation (27) provides a CRSS  $\approx 140$  MPa. This value is much larger than the one given by Equation (25) and is closer to the experimentally measured value. This equation also indicates that the yield strength is dependent only on the internal coherency strains and independent of the wavelength of composition modulation. However, in spite of the better agreement with experimental data, Dahlgren's theory does not seem to be acceptable either [10], as he tacitly assumed a straight dislocation to obtain Equation (27). Due to the existence of an internal stress field, the assumption of a straight dislocation is not valid.

### 2.3 Theory by Carpenter

Carpenter [6], and as well as Ditchek and Schwartz [8] have proposed the lattice mismatch theories to explain the age-hardening of spinodal alloy. They considered the mismatch between lower and upper halves of a slip plane due to the difference in the lattice parameter when a dislocation cuts through the modulated structure. It is believed that the idea of the lattice mismatch is equivalent to the consideration of coherency stress if the continuum

elastic theory is applied. As a result, their theories correspond to the consideration of the contribution of the coherency internal stress using a different approximation. According to Carpenter [6], the yield stress is given as

$$\sigma = \frac{(\Lambda\eta)^2 E^2}{2\pi\sqrt{6}Gb} \quad \text{for screw dislocations,} \quad (28)$$

and

$$\sigma = \frac{(\Lambda\eta)^2 E^2}{2\pi\sqrt{2}Gb} \quad \text{for edge dislocations.} \quad (29)$$

Where "G" is the shear modulus and "E" is the Young's modulus. Similar to Cahn's theory [3], Carpenter's model also predicts  $\Lambda^2$  dependence of the yield stress for both screw and edge dislocations. Since Carpenter [6], as well as Ditchek and Schwartz [8], have neglected the important role of the dislocation self stress, their theories are not considered to be satisfactory [10].

#### 2.4 Theory by Ghista and Nix

Ghista and Nix [7] have suggested that the elastic inhomogeneity, i.e., the spacial variation of the elastic modulus, in the modulated alloy is responsible for the age-hardening effect. From their theory, the CRSS required for dislocation movement is

$$\sigma = \left( \frac{P}{E} \right) \bar{G} b \left( \frac{1.75 \times 10^{-3}}{\lambda} \right), \quad (30)$$

where "P" is the force intensity on a dislocation, " $\bar{G}$ " is the average shear modulus and  $\bar{E} = \bar{G}b^2$ . This equation suggests that the CRSS increases linearly with the amplitude of the variation in shear modulus and inversely with the wavelength. Their theory was also proven to be unrealistic [10]. They have only considered a straight dislocation and neglected the contribution by the internal coherency stress. In addition, even when the Bessel function approximation of the radial variation of the shear modulus is permitted to appear in their theory [7], one cannot rely on their calculation based on the assumption that the resultant self energy of the dislocation is also a damping function of the position. Since, according to their model, the elastic inhomogeneity is distributed periodically, the self energy of the dislocation should also be a completely periodic function of the position.



## 2.5 Theory by Ditchek and Schwartz

Ditchek and Schwartz [2] have obtained an empirical equation of age-hardening. According to them, the incremental yield stress,  $Y_s$ , in spinodal alloys can be expressed as

$$Y_s = \alpha_1 A + \alpha_2 A (\lambda - \lambda_0) / \lambda, \quad (31)$$

where " $\alpha_1$ ", " $\alpha_2$ ", and " $\lambda_0$ " are constants depending on the material itself. Equation (31) is based on the experimental results on Cu-10Ni-6Sn alloy by Ditchek and Schwartz [42] and it considers earlier and as well as later stages of decomposition. According to their experiments the amplitude " $A$ " initially increases rapidly as the aging time increases, while the wavelength " $\lambda$ " remains almost constant during the early stages of decomposition. This predicts that the increase in yield stress, at least initially, is proportional to " $A$ ". In fact, Butler and Thomas [24], in their experiment using Cu-Ni-Fe alloy, have observed that the yield stress is proportional to " $A$ " and is independent of " $\lambda$ ".

Since Equation (31) is empirical, and " $\lambda$ " begins to increase only at the later stages of decomposition,  $Y_s$  should be affected by wavelength " $\lambda$ " only at later stages of decomposition. However, at later stages, the modulation profile can no longer be assumed to be sinusoidal [22].

Equilibrium coexistence of two-phases should be observed ultimately, and the modulation wave in this case can only be expressed in terms of Fourier series. Hence, it is still doubtful whether Equation (31) is applicable regardless of the stages of decomposition.

## 2.6 Theory by Hanai et al.

Hanai et al. [9] explained the age-hardening mechanism in spinodal alloys with a model based on the evaluation of interfacial energy per unit area of the slip plane. They proposed that new interfaces are produced on the slip plane when a crystal with continuous composition fluctuations is deformed by slip. They evaluated the energy of such interfaces for modulated structures, and concluded that the contribution of the interfacial energy is large enough to account for the age-hardening concomitant with spinodal decomposition.

Hanai et al. [9] proposed that the yield stress is proportional to the square of the amplitude and to the inverse of the wavelength of the composition modulation. For FCC structure

$$\sigma = (4\sqrt{2}\pi/9)\{2U_e n_c n_s + kG\Omega^2\}A^2\lambda^{-1} \quad (32)$$

for screw dislocations, and

$$\sigma = (\sqrt{6}\pi/3) \{2U_e n_c n_s + kG\Omega^2\} A^2 \lambda^{-1} \quad (33)$$

for edge dislocations, where  $U_e$  is the interchange-energy of atom pairs,  $n_s$  is the co-ordination number,  $n_c$  is the number of atoms per unit area of the interface and "k" is a constant related to the shape of the solute rich region.

Unfortunately, there are several drawbacks in this theory [10]. Firstly, they considered the interfacial energy to be the sum of chemical interfacial energy and elastic strain energy. Interfacial energy is defined per unit area whereas elastic strain energy is defined per unit volume. Secondly, they overestimated the interfacial energy to be 0.3 J/m<sup>2</sup>. This overestimation arises since the modulated structure in spinodal alloys is characterized by the fluctuation of constitutive atoms and is not brought about by an entirely different atomic arrangement. Therefore, this theory is not considered to be satisfactory.

## 2.7 Theory by Kato, Mori and Schwartz (K-M-S Theory)

Kato, Mori and Schwartz [10] proposed a theory to understand the age-hardening mechanism in spinodal alloys. Based on the force-balance equation, Equation (16), Kato et al. considered a mixed dislocation (having its Burgers vector at 60° to the dislocation line direction) instead of

pure edge and screw dislocations, to be responsible for the macroscopic yielding in FCC spinodal alloys. This is because the free energy per unit length of such a mixed dislocation is smaller than that of the edge or screw dislocation in specimens that have undergone spinodal decomposition. As a result, the mixed configuration of dislocation is believed to be energetically favorable. The macroscopic yielding in the modulated structure is assumed to be controlled by the motion of the mixed dislocations having the minimum energy, and experience the largest resistance from the internal stress field.

To describe the mixed dislocation configuration, a new coordinate system  $(u, v)$  is introduced so that the dislocation line lies parallel to the  $u$ -axis, i.e.,

$$\begin{aligned} u &= \frac{x}{\sqrt{2}} - \frac{y}{\sqrt{6}} - \frac{\pi}{\beta}, \\ v &= \frac{x}{\sqrt{2}} + \frac{y}{\sqrt{6}}. \end{aligned} \quad (34)$$

The force field due to the composition modulation, with the above transformation, is shown in Figure 3. Equation (16) can now be rewritten as

$$\frac{\sqrt{6}}{\sqrt{4} \left[ 1 + \left( \frac{dv}{du} \right)^2 \right]^{3/2}} \Gamma \left( \frac{d^2 v}{du^2} \right) + \frac{1}{\sqrt{6}} \Delta \gamma b [\cos(\beta u) + \cos(\beta v)] + \sigma b = 0. \quad (35)$$

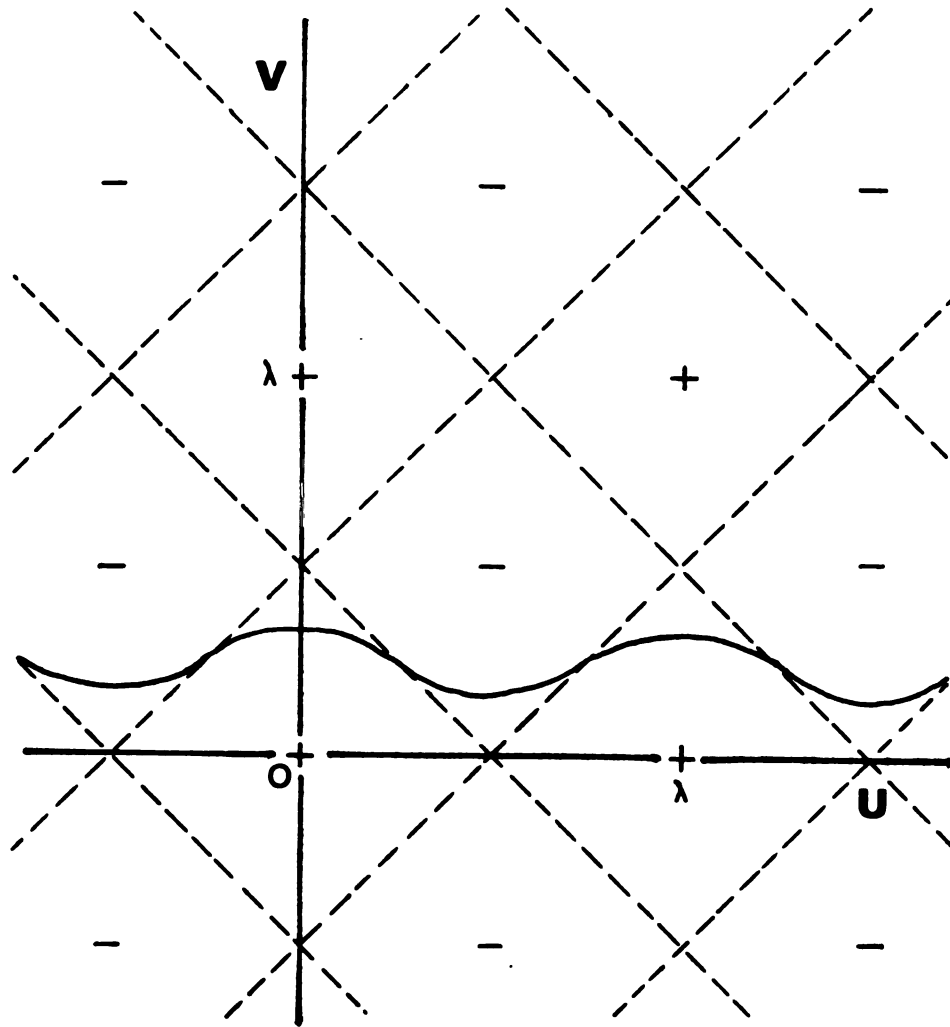


**Figure 3** Schematic representation of the force field on mixed dislocations  $[10]$ .

To solve this nonlinear second order differential equation, an approach similar to that of Cahn was adopted. By assuming the slope of the dislocation line to be very small, the derivatives in the denominator of the first term in Equation (35) were neglected. The stable shape of the dislocation was assumed to be cosinusoidal, i.e.,

$$v = C_1 + C_2 \cos(\beta u) , \quad (36)$$

where  $C_1$  and  $C_2$  are the unknown parameters to be determined. Adopting the Galerkin method, just as in Cahn's analysis,  $C_1$  and  $C_2$  are obtained as

$$\begin{aligned} \cos(\beta C_1) &= - \frac{\sqrt{6}\sigma}{A\eta Y} , \\ C_2 &= \frac{6A\eta Y b \Gamma \beta - 4A\eta Y b^2 \sqrt{A^2 \eta^2 Y^2 - 6\sigma^2}}{(24\sigma^2 b^2 + 9\Gamma^2 \beta^2 - 4A^2 \eta^2 Y^2 b^2) \beta} . \end{aligned} \quad (37)$$

As Equation (37) indicates that, if  $|\sigma|$  is larger than  $A\eta Y/\sqrt{6}$ , no stable solution can exist. Under such conditions the CRSS can be written as

$$\sigma = A\eta Y/\sqrt{6} . \quad (38)$$

This value corresponds to the incremental CRSS in the aged spinodal alloy [10]. The theoretically predicted values of

incremental CRSS based on this model, as compared to Cahn's model, are in closer agreement with the experimentally measured ones [10].

## 2.8 Theory by Ardell

More recently, Ardell [11] criticized that the theories of Cahn [3] and Kato et al. [10] are both too primitive in the sense that they both predict the CRSS of an ideal microstructure. Furthermore, Ardell criticized that according to K-M-S theory the CRSS is entirely independent of the characteristic of the dislocation line, i.e., independent of " $b$ " and " $\lambda$ ". This cannot be considered to be reasonable.

In his approach, the microstructure of alloys hardened by spinodal decomposition is modulated, but not perfectly periodic. Furthermore, the hardening mechanism is considered to be due to the interaction between dislocation and diffused obstacles, i.e., the interaction between them is not localized but they can interact with each other at a distance. This consideration was first proposed by Mott [43]. Mott's treatment was one of the earliest to recognize the role of dislocation flexibility in the determination of the spacing of obstacles along the dislocation line. Mott dealt with a single dislocation interacting with attractive obstacles at zero applied stress. This interaction causes

the dislocation to assume a zig-zag configuration shown in Figure 4.

By minimizing the total energy of the dislocation line in the zig-zag array of obstacles and considering the influence of an applied stress on the dislocation line, the critical stress,  $\tau_c$ , required for the dislocation to break free from the obstacles can be written as

$$\tau_c = \frac{2\Gamma v^{1/3} \beta_c^{4/3}}{b L_o^{4/3}}, \quad (39)$$

where "v" and " $\beta_c$ " are the amplitude and the maximum slope of the dislocation line respectively, and " $L_o$ " is the spacing between obstacles. In the case of spinodal decomposition, the values of " $\beta_c$ " and "v" were obtained from the solution of Cahn [3] for the periodic shape of the edge dislocation. The reason for choosing the edge dislocation is that the resulting value of  $\tau_c$  provided the best agreement with the limited experimental data available. From Cahn's solution, the values of " $\beta_c$ " and "v" are

$$\beta_c = \frac{\Delta\gamma b \lambda}{\sqrt{2\pi}\Gamma}, \quad \text{and} \quad (40)$$

$$v = \frac{\sqrt{3}\Delta\gamma b \lambda^2}{2\pi^2\Gamma}. \quad (41)$$



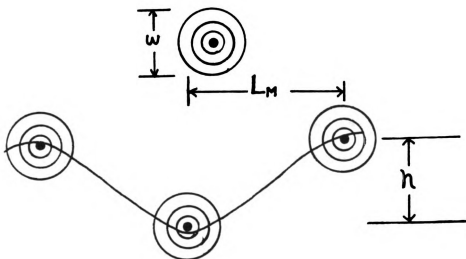


Figure 4 Illustration of the basic geometry of Mott statistics [43]. " $L_M$ " is the Mott's spacing, " $w$ " is the range of interaction between an obstacle and a dislocation, and " $h/2$ " is the amplitude of the zig-zag dislocation configuration.

Substitution of Equations (40) and (41) into Equation (39), with  $L_s = \lambda$ , results in

$$\tau_c = 0.122(A\sigma Y)^{2/3}(\lambda b/\Gamma)^{2/3} \quad . \quad (42)$$

The numerical coefficient in Equation (42) depends upon the character of the dislocation. Since this numerical coefficient is largest and " $\Gamma$ " is smallest for edge dislocations,  $\tau_c$  is significantly higher for edge dislocations than for mixed or screw dislocations. Equation (42) also predicts a dependence of the CRSS on " $A$ " and " $\lambda$ " which is somewhat less strong than that predicted by Cahn's theory.

## CHAPTER 3

### EXPERIMENTAL PROCEDURE

#### 3.1 Specimen Preparation

The stock material used in the present study is a Cu-10Ni-6Sn alloy obtained from Bell Laboratories. Flow chart for specimen preparation is shown in Figure 5. Schematic of electropolishing steps used in producing tensile specimens for in-situ deformation are shown in Figure 6. Solutions and operating conditions used for chemical thinning and electropolishing are shown in Table 1.

As received stock was rolled down to 0.5 mm thickness using a cold rolling mill. Rectangular strips (4.0 cm x 0.7 cm) were cut out from the as-rolled sheet. Homogenizing was carried out by solution-treating these rectangular specimens at 1073 K for 3 minutes and drop quenching in water in order to remove all the residual stresses caused by prior mechanical working. Grain growth was achieved by using a strain-annealing method. In this method, specimens were

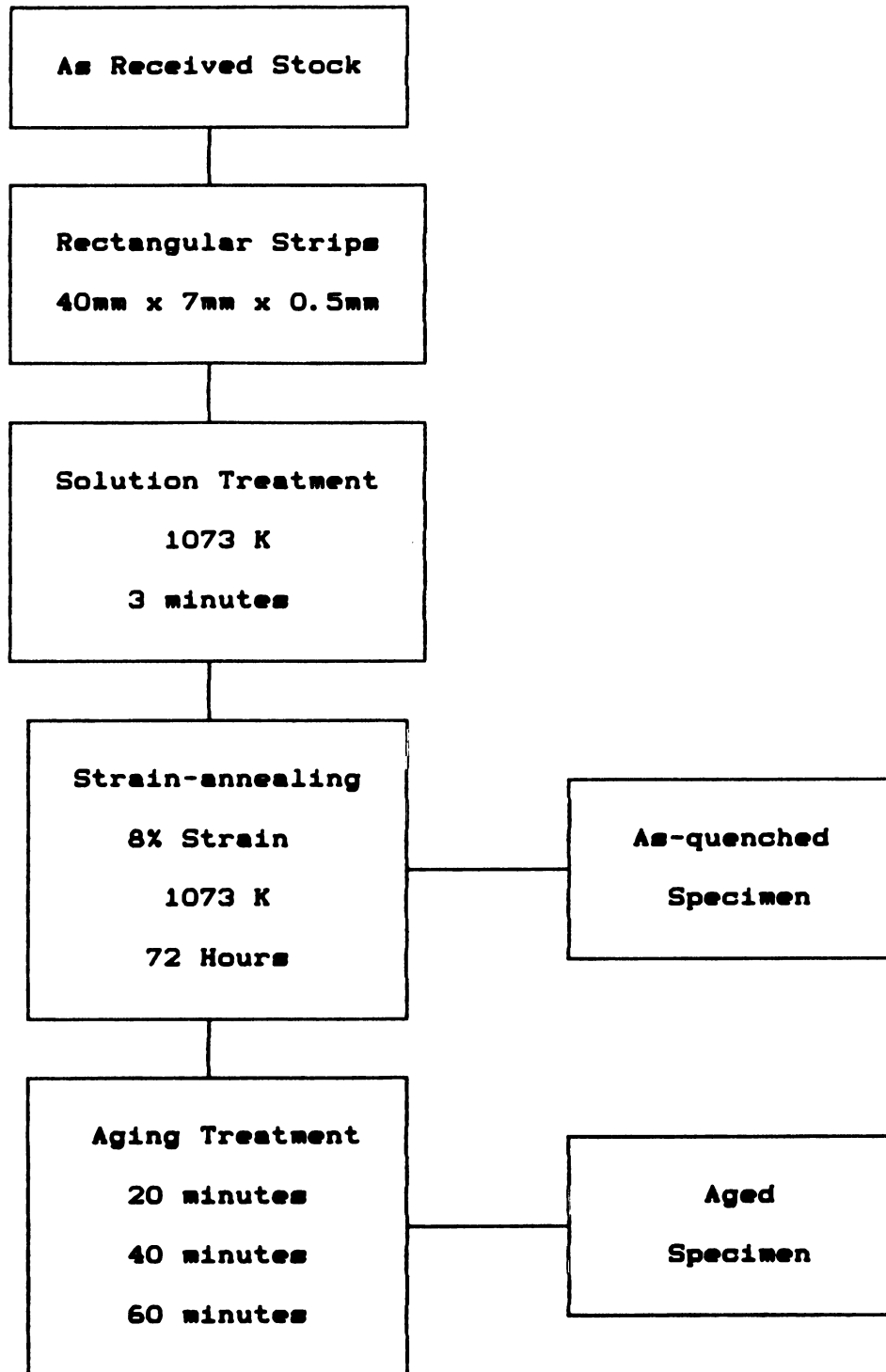


**Figure 5 Thermal and Mechanical treatment flow chart for specimen preparation.**

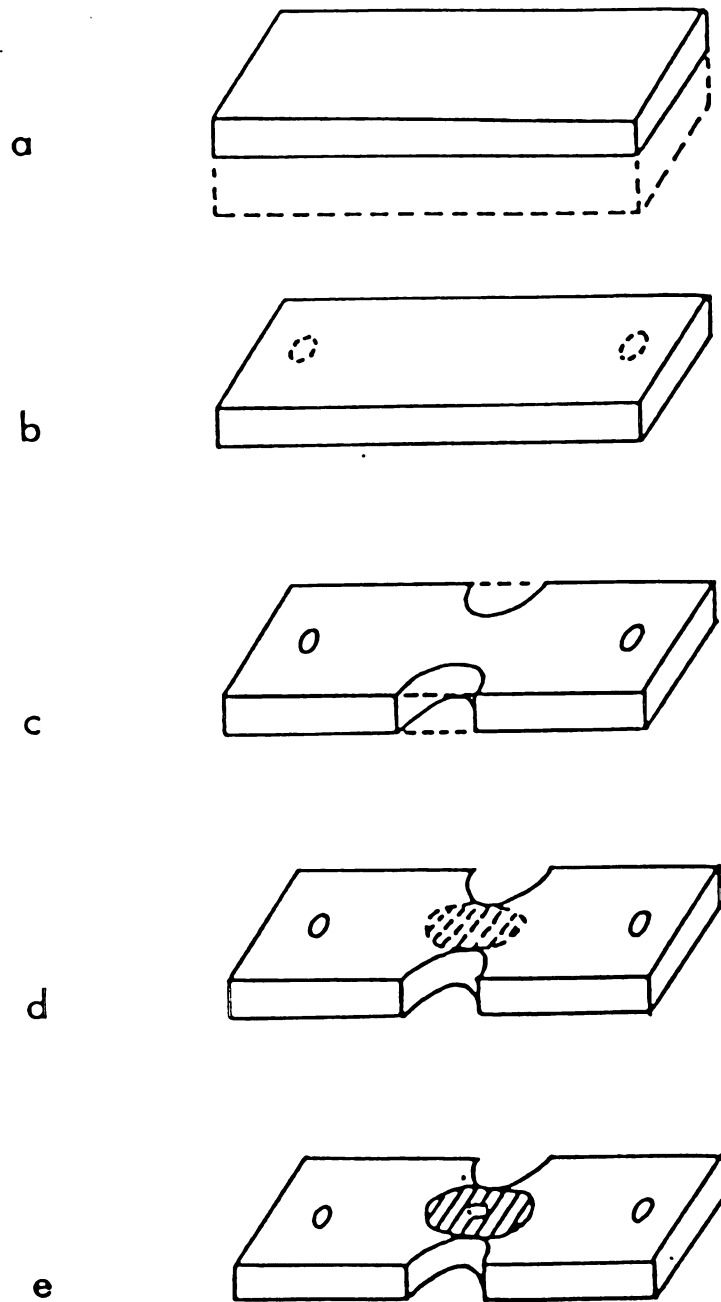


**Figure 6** Schematic representation of electropolishing steps in preparation of specimens for in-situ straining in HVEM.

**Table 1 Chemical thinning and electropolishing data for the preparation of specimens for in-situ straining.**

<b>Polishing Step</b>	<b>Electrolyte Composition</b>	<b>Voltage Volt(s)</b>	<b>Temperature (K)</b>
<b>Chemical Thinning</b>	40% Nitric Acid 60% Distilled Water	0	293
<b>Gage Section</b>	20% Nitric Acid 80% Methanol	50	293
<b>Concave Surfaces</b>	20% Nitric Acid 80% Methanol	50	233
<b>Perforation</b>	20% Nitric Acid 80% Methanol	8	233

imparted a critical strain of 8% and annealed at 1073 K for 72 hours in vacuum followed by drop quenching in water. Specimens that did not receive any additional heat treatments are referred to as "as-quenched specimens" in this study. Some of the as-quenched specimens were aged at 623 K for 20, 40 and 60 minutes in order to induce varying extents of composition modulation, and drop quenched in water following the aging treatments. These specimens are referred to as "aged specimens" in this study.

After finishing all the necessary heat treatments as mentioned above, specimens were thinned down to about 100  $\mu\text{m}$  by chemical polishing using a 40% nitric acid and 60% distilled water solution (Table 1). After thinning, rectangular strips (9 mm x 3 mm) were cut out as shown in Figure 6(a). Two holes were drilled 6.5 mm apart at either end of the strip to facilitate mounting of the specimen onto the straining device of the HVEM as shown in Figure 6(b). Using a solution of 20% nitric acid and 80% methanol, maintained at room temperature (Table 1), the long edge of the strips were electropolished away so as to produce the gage section of the tensile specimen as shown in Figure 6(c).

The central portion of the specimen was made transparent to the electron beam by using a two-step electropolishing method. In the first step, as shown in Figure 6(d), jet

polishing was performed to produce concave surfaces on both sides of the specimen. Apparatus used for this jet polishing process is shown in Figure 7. Specimen was placed on the platinum wire under the jet stream of the electrolyte. After polishing for about 30 seconds, specimen was turned over and the polishing was resumed on the other side of the specimen for the same length of time. The main purpose in producing concave surfaces on both sides of the specimen was to produce electron transparent regions in the central portion of the specimen during the second step of the electropolishing. Electropolishing solution and polishing conditions used in this step are given in Table 1. In the second step, the specimen was electropolished to produce the perforation as shown in Figure 6(e), using the same solution and temperature conditions as that for the first step. However, the electropolishing voltage and current density were different as compared to the first step (Table 1). Apparatus used for this final polishing process is shown in Figure 8. Specimen holder was made by connecting two platinum loops at the tip of a reversed-action tweezer and the specimen was held between these two platinum loops. Cathode was made of a cylindrical stainless steel sheet with cut out slots. A pointed light source was used to determine when perforation occurred in the center of the gage section. As soon as a hole was formed, the specimen was removed from the electrolyte and washed thoroughly in running methanol. This final step was



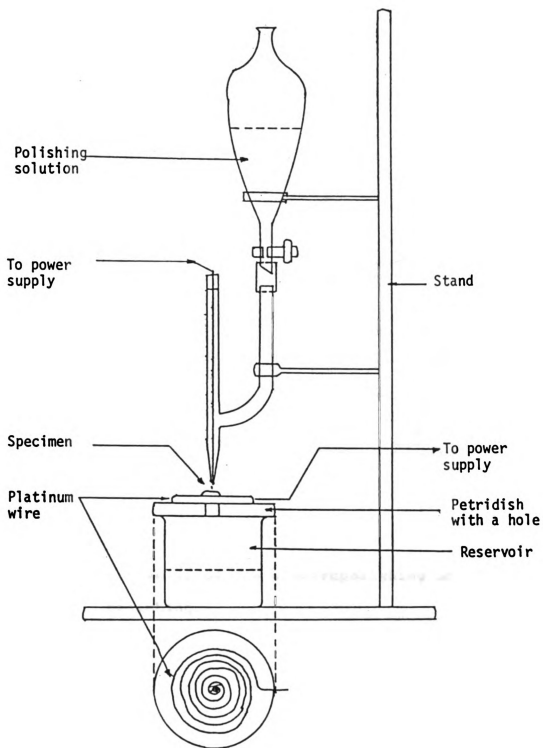


**Figure 7 Schematic of the electropolishing unit for jet polishing.**

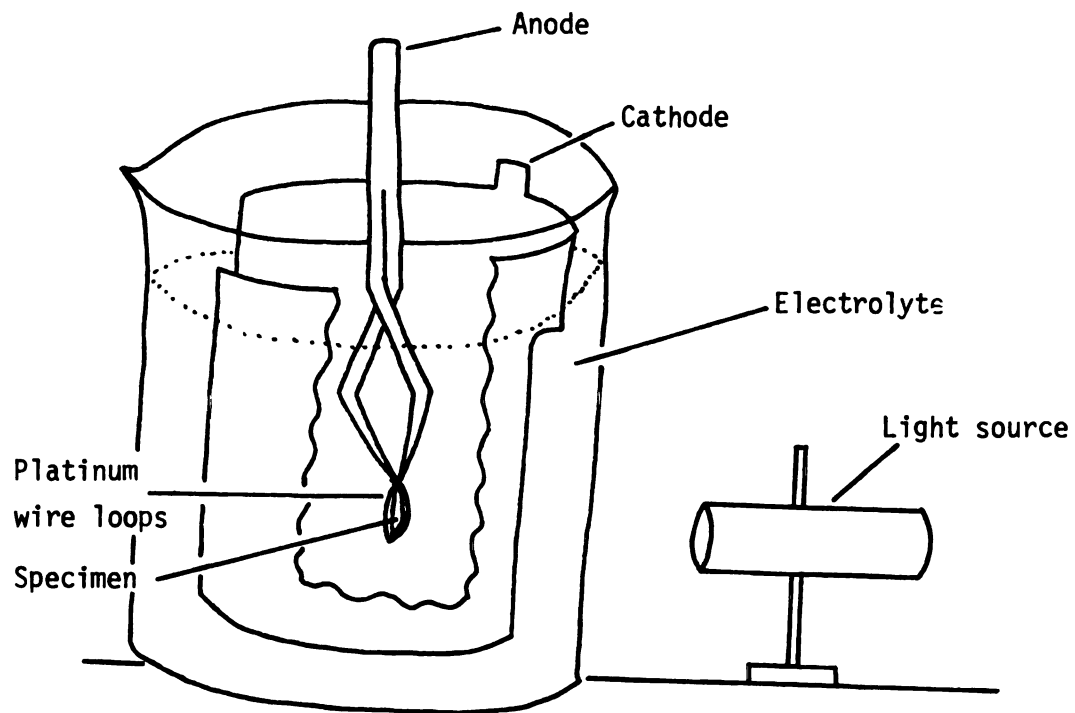


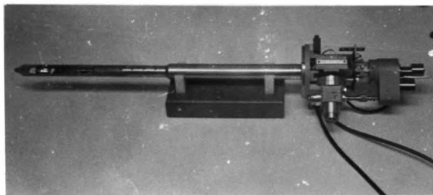
**Figure 8 Schematic of the electropolishing unit for final polishing.**

always carried out just prior to insertion of the specimen in HVEM so as to avoid any possible oxidation and contamination problems.

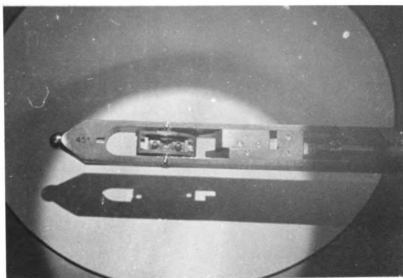
### 3.2 In-situ Deformation in HVEM

In-situ deformation was carried out by using HVEM at Argonne National Laboratories (ANL). Straining was imparted by means of an electric motor attached to the specimen stage provided with double tilting capabilities as shown in Figure 9(a). A specimen mounted on this straining device can be seen in Figure 9(b). Deformation rate of this straining device was controlled by adjusting the voltage applied to the straining motor. Figure 10 is a plot of deformation rate versus applied voltage. With a  $\pm 40^\circ$  tilting capability along both tilting axes, this device is suitable for carrying out the required Burgers vector analysis of dislocations that were observed to move during straining.

HVEM at ANL is capable of operating with accelerating voltages upto 1.2 million volts. However, based on the critical voltage for copper, radiation damage may become a serious problem at accelerating voltage higher than 450 KV. As shown in Figure 11, specimen observed with an accelerating voltage of 1 MV revealed extensive radiation damage with increasing electron irradiation. On the other hand, specimens studied with an accelerating voltage of 400



(a)



(b)

Figure 9 (a) The Gatan double-tilt microtensile stage for in-situ straining in HVEM.

(b) Photograph of a specimen mounted on the microtensile stage.

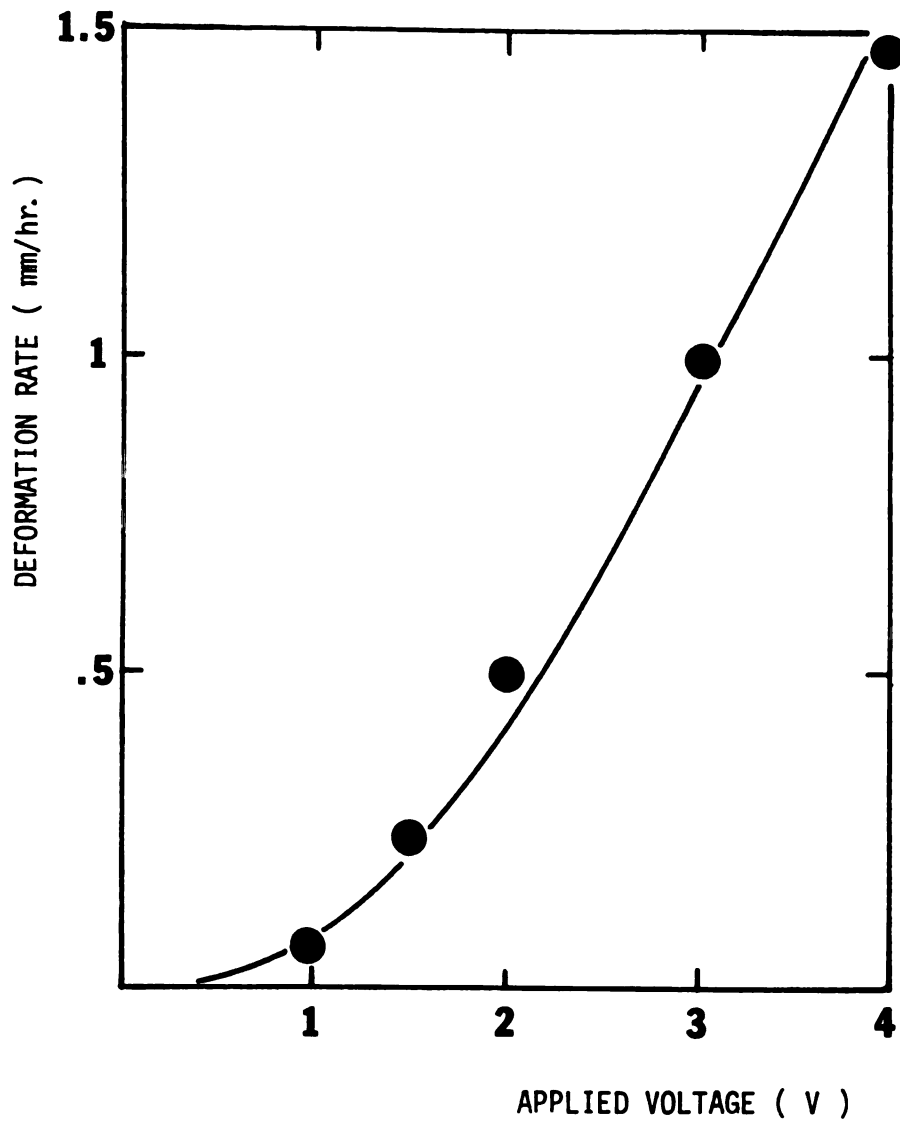
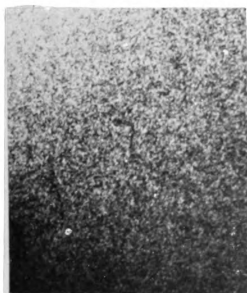


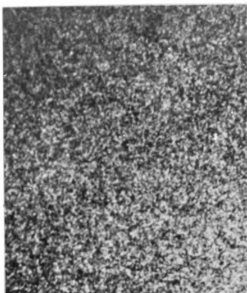
**Figure 10** The deformation rate versus applied voltage curve of the Gatan microtensile stage.



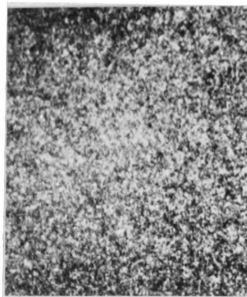
(a)



(b)



(c)



(d)

**Figure 11 Radiation damage in a specimen examined at 1 MV over a time period of 12 minutes.**

(a)  $t = 0$  minute

(b)  $t = 1$  minute

(c)  $t = 3$  minutes

(d)  $t = 12$  minutes.

KV did not reveal any observable radiation damage within reasonable length of time. This accelerating voltage is below the critical voltage for copper. As a result, all the in-situ straining investigations were carried out with an accelerating voltage of 400 KV. In order to minimize thin film (surface) effects, observations were always attempted in regions far away from the edge of the perforation. Dynamic dislocation events that occurred during deformation were recorded by using a video camera located beneath the viewing screen of the microscope. Conventional spot film technique was also used to carry out Burgers vector analysis.

The usual procedure in performing the in-situ deformation is as follows: Straining was started after inserting the specimen into the specimen chamber of the microscope. Deformation rate was kept as low as possible (usually at 0.5 mm/hr.) in order not to miss any dislocation activity while scanning over the thin regions of the specimen. As soon as the motion of dislocations were noticed, viewing screen was lifted up and these dislocation movements were recorded on the video tape. After successful recording of these dynamic dislocation events to the required extent, straining device was stopped. However, the video recording was still continued to document the dislocation rearrangement that occurred due to the residual stresses. As soon as the dislocation rearrangement stopped,

video recording was also discontinued and Burgers vector analysis on these dislocations was carried out.

"Two-beam condition" method was used for the Burgers vector analysis in the present study. With this method, it is necessary to obtain a series of images of the same field of view with a number of specific diffracting conditions operating separately. This was carried out by tilting the specimen so that the incident beam direction was close to one of the major zone axes. Specimen was further tilted by a small amount of  $5^\circ$  to  $10^\circ$  about different axes to obtain a series of two beam conditions in the diffraction pattern. Diffraction vectors,  $\vec{g}$ , were determined from these two beam conditions. This tilting was performed in the selected area diffraction mode, only occasionally returning to the image mode to check if specimen had moved from the region of observation. After obtaining a series of micrographs of bright field images together with their corresponding diffraction patterns, the " $\vec{g} \cdot \vec{b} = 0$  criterion" was applied to determine the direction of the Burgers vector,  $\vec{b}$ . This is because dislocation became invisible when its Burgers vector is lying on the reflecting plane. Two such invisibility conditions suggest that  $\vec{b}$  is common to both reflections, and that  $\vec{b}$  must be the zone axis of the two reflecting planes.

Dislocation line direction was determined by conducting trace analysis on stereographic projection. Since the



Burgers vector of a dislocation is always lying on its slip plane, from the results of Burgers vector analysis, possible slip planes can be determined. Great circles representing these slip planes were drawn on the stereographic projection. Since the image of a dislocation on the micrograph is actually a projection of this dislocation on a two-dimensional plane, true direction of this dislocation can be determined by using a straight line parallel to this projected direction and pathing through the center of the stereographic projection. By intersecting this straight line with the great circle of the slip plane on the stereographic projection, direction of the dislocation line was determined. Knowing the direction of the dislocation line and its Burgers vector, the character of this dislocation can be determined.

## CHAPTER 4

### EXPERIMENTAL RESULTS

General aspects concerning the motion and the character of mobile dislocations observed during the HVEM in-situ deformation studies are presented in this Chapter. In general, the observed motion of dislocations can be roughly divided into two categories, namely, individual motion and collective motion. Since macroscopic yielding is mainly controlled by the collective motion of dislocations on the slip plane with the maximum resolved shear stress, observations and analyses presented in this chapter will be on such dislocations. As mentioned in the previous chapter, almost all of the specimens were strained at the lowest possible deformation rate,  $\approx 0.5$  mm/hr.

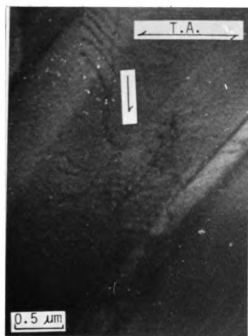
#### 4.1 General Observations

In this section, results based on the observations of dynamic dislocation events that occurred during in-situ straining in as-quenched and aged specimens are presented.

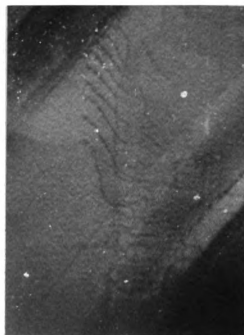
It was noted that in all the cases the mobile dislocations observed were nucleated during straining; pre-existing dislocations were relatively immobile during in-situ deformation. The character of these mobile dislocations has been analyzed in Section 4.2 for some of the cases presented in this section.

In as-quenched specimens, mobile dislocations glide smoothly. The velocity of these dislocations was found to be constant in a given slip plane at a given deformation rate. In Figure 12, the orientation of the dislocations present in the slip trace varies from almost parallel to the tensile axis (marked as "T.A.") in the lower part of the micrographs to almost perpendicular to the tensile axis in the upper part of the micrographs. The overall motion of the dislocations is indicated by the arrow in Figure 12(a). The changes that can be observed in these micrographs occurred during a period of 20 seconds.

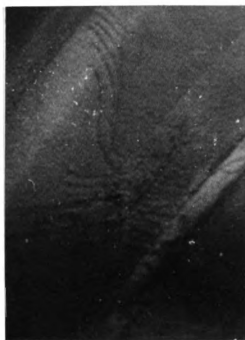
The dislocations marked "1", "2", "3" and "4" in the series of micrographs of Figure 13 glided along the slip trace without any particular change in orientation. Rearrangement to a small extent of the dislocations indicated as "1", "2" and "3" can be seen in the micrographs of Figure 14. The dislocation activity along the slip trace marked "ST" in Figure 15 was so violent that it was impossible to resolve the motion of individual dislocations



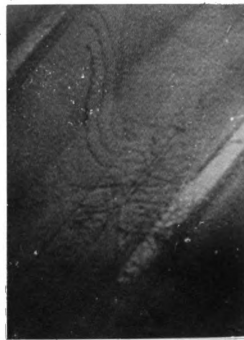
(a)



(b)

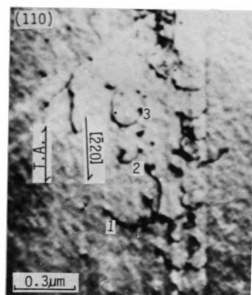


(c)

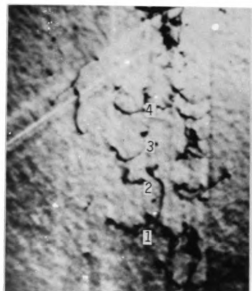


(d)

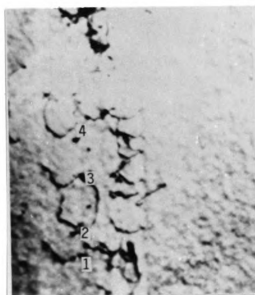
Figure 12 Series of micrographs showing motion of dislocations along slip traces in homogenized specimen during in-situ deformation in HVEM.



(a)



(b)

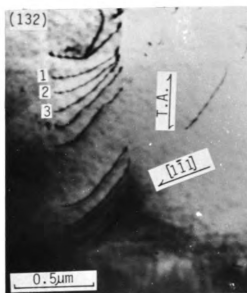


(c)



(d)

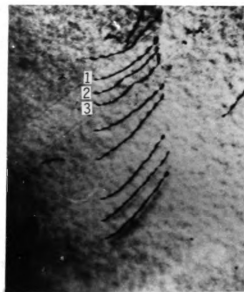
**Figure 13** Series of micrographs showing motion of dislocations along slip traces in homogenized specimen during in-situ deformation in HVEM.



(a)



(b)



(c)

Figure 14 Series of micrographs showing motion of dislocations along slip traces in homogenized specimen during in-situ deformation in HVEM.

during the time period of activity. These four micrographs have been taken from the video recordings. Dislocations in Figures 14 and 15 have been analyzed for their character and are presented in Figures 30 and 28 in Section 4.2.

Micrographs of four sets of dislocations that were mobile during deformation in specimens aged for 20 minutes are given in Figures 16 through 19. In Figure 16, the dislocations lying along the slip trace marked "ST" were observed to move from left to right as indicated by the arrow. The motion was less smooth than that in homogenized specimens. In Figure 17, dislocations marked "1", "2", "3" and "4" were observed moving along the slip trace marked "ST" in a similar manner. The characters of these dislocations have been analyzed and are presented in Figure 34 in Section 4.2.

The progression of dislocations over a period of 30 seconds along the slip trace marked "ST1" are shown in the micrographs of Figure 18. The motion of the leading dislocation was very discontinuous. With increasing amount of deformation, slip in "ST1" progressed in bursts and intersected the slip trace marked "ST2". In Figure 19, dislocations marked "1" and "2" were observed to move along the direction indicated by the arrow. All the dislocations presented in these micrographs in Figure 19 emanated from dislocation sources along the edge of the specimen and were

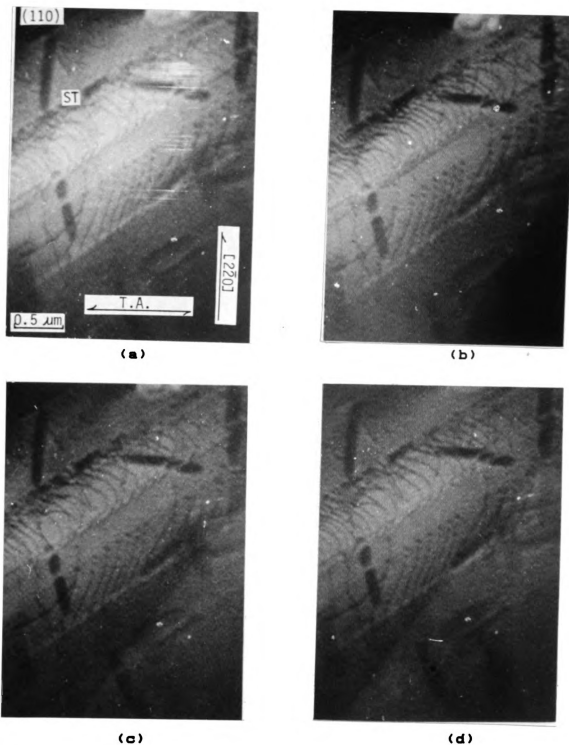
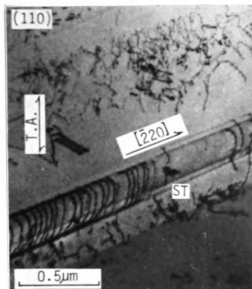
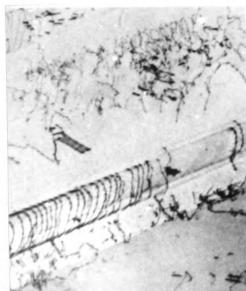


Figure 15 Series of micrographs showing motion of dislocations along slip traces in homogenized specimen during in-situ deformation in HVEM.





(a)



(b)

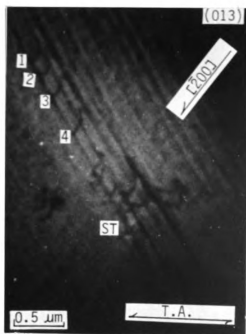


(c)

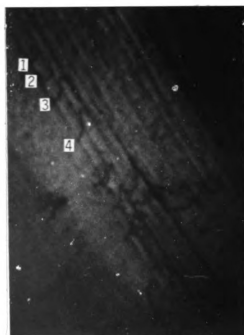


(d)

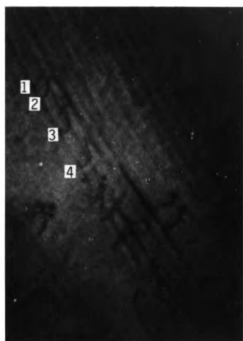
Figure 16 Series of micrographs showing motion of dislocations along slip traces in an aged specimen during in-situ deformation in HVEM. Specimen aged at 623 K for 20 minutes.



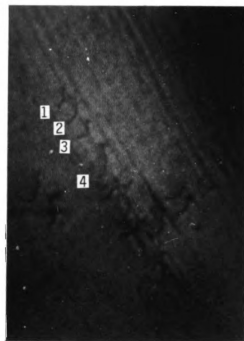
(a)



(b)

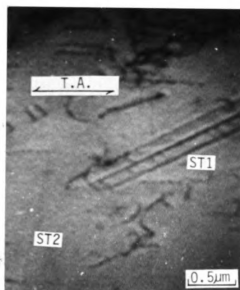


(c)

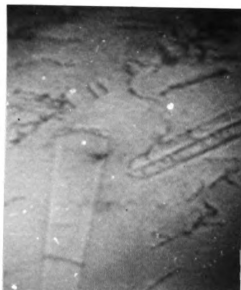


(d)

Figure 17 Series of micrographs showing motion of dislocations along slip traces in an aged specimen during in-situ deformation in HVEM. Specimen aged at 623 K for 20 minutes.



(a)



(b)



(c)



(d)

Figure 18 Series of micrographs showing motion of dislocations along slip traces in an aged specimen during in-situ deformation in HVEM. Specimen aged at 623 K for 20 minutes.

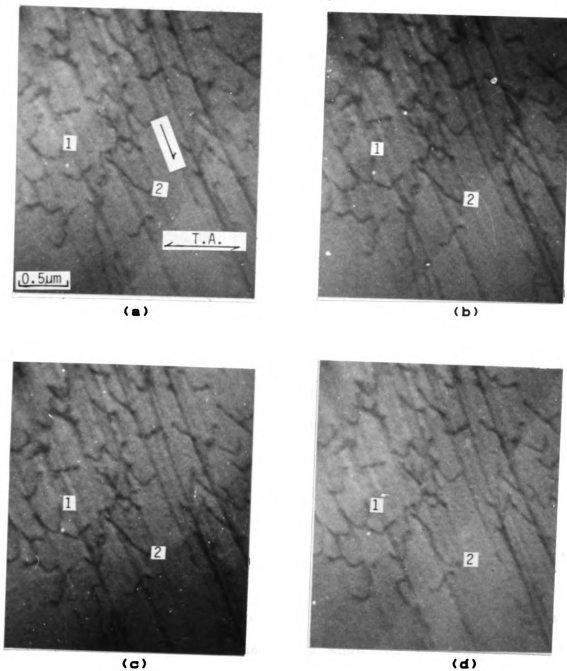


Figure 19 Series of micrographs showing motion of dislocations along slip traces in an aged specimen during in-situ deformation in HVEM. Specimen aged at 623 K for 20 minutes.

observed to move along parallel slip traces.

The motion of dislocations along slip traces during the in-situ straining of specimens aged for 20 minutes can be best described as follows: The leading dislocations tend to bulge along parts of their length in the direction of motion. This was followed by the rest of the dislocation moving forward to reduce the overall length. Whereas the motion of the leading dislocations was discontinuous, the trailing dislocations glided relatively smooth along the slip trace.

In specimens aged for 40 minutes, the behavior of the dislocations was very irregular and can be classified into two categories. In some cases, all the dislocations present in slip traces were observed to move in a discontinuous manner, with alternating periods of rest and motion. In other cases, dislocations were observed to move in a manner similar to that in specimens aged for 20 minutes.

Micrographs of two sets of dislocations that were mobile during deformation in specimens aged for 40 minutes are given in Figures 20 and 21. Contrast due to the composition modulation is evident in the micrographs presented in Figure 20. All the dislocations along the slip trace were observed to move in a jerky manner. This jerky motion can be described in a manner similar to that of the leading dislocations in specimens aged for 20 minutes. This

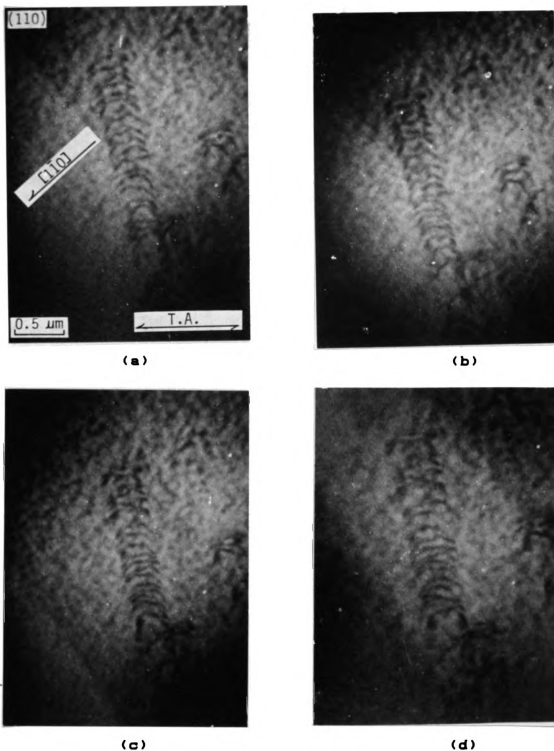


Figure 20 Series of micrographs showing motion of dislocations along slip traces in an aged specimen during in-situ deformation in HVEM.

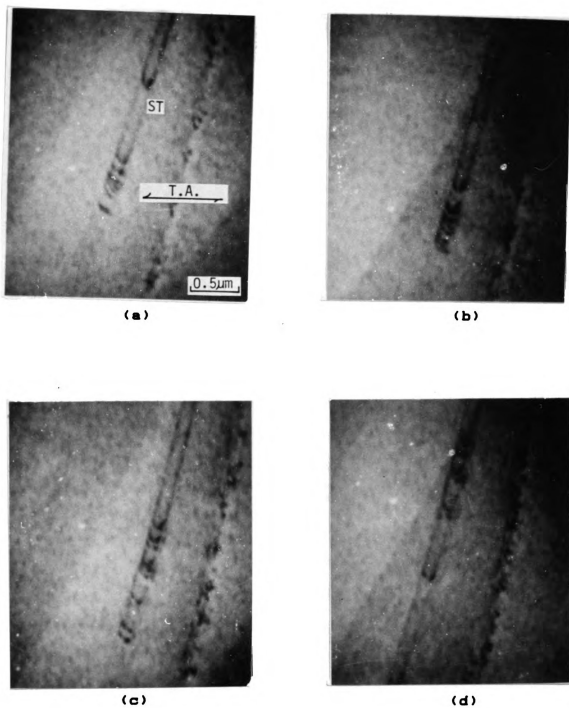


Figure 21 Series of micrographs showing motion of dislocations along slip traces in an aged specimen during in-situ deformation in HVEM. Specimen aged at 623 K for 40 minutes.

phenomenon is repeated a number of times as the dislocations moved along the slip trace. Dislocations presented in the micrographs of Figure 21 were observed to progress along the slip trace marked "ST" over a period of 20 seconds. In this case, only the leading dislocation was observed to move in a discontinuous manner. The following dislocations glided relatively easier.

For specimens aged for 60 minutes, all the mobile dislocations present in the slip traces were seen to move in a jerky manner with alternating periods of rest and motion. This behavior is clearly illustrated in the micrographs of Figure 22, where these dislocations can be observed to move in parallel slip traces along the direction indicated by the arrow. Similar behavior was also found for dislocations presented in micrographs of Figure 23, where the dislocations moved discontinuously along the single slip trace. Long dislocations that have changed their orientation by bulging out from their original position can be seen in Figure 24. This phenomenon is very similar to the theoretically predicted double-kink formation during motion of dislocations in the stress field due to spinodal decomposition [44]. Analysis of the character of these dislocations is given in Section 4.2.

Crack formation due to excessive deformation was also observed although this aspect was not of main interest in



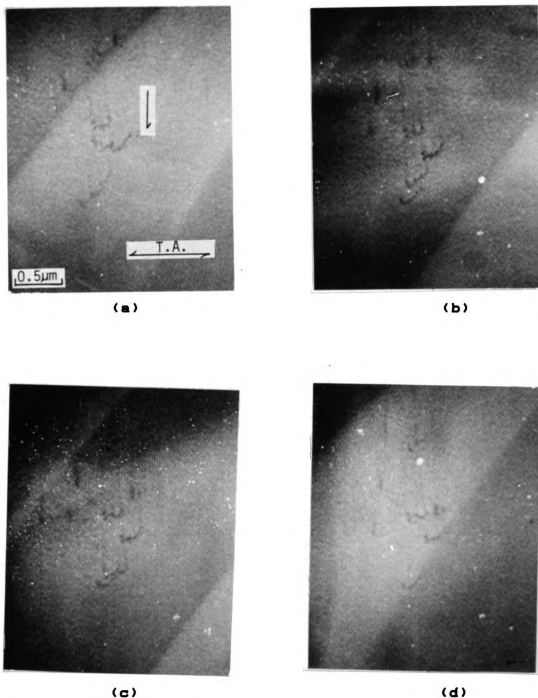
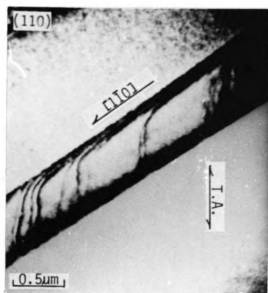
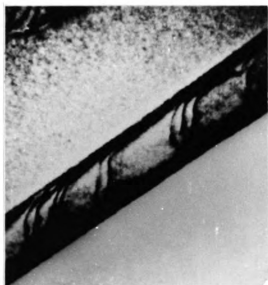


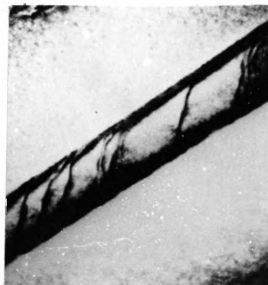
Figure 22 Series of micrographs showing motion of dislocations along slip traces in an aged specimen during in-situ deformation in HVEM. Specimen aged at 623 K for 60 minutes.



(a)



(b)



(c)

Figure 23 Series of micrographs showing motion of dislocations along slip traces in an aged specimen during in-situ deformation in HVEM. Specimen aged at 623 K for 60 minutes.

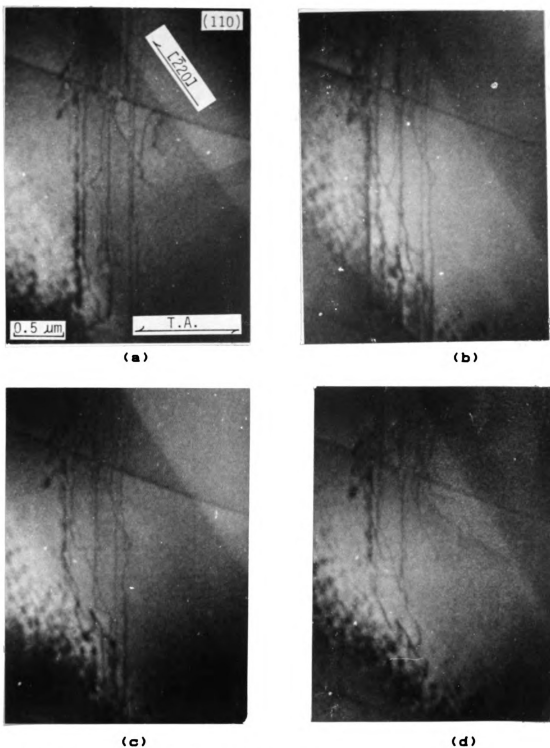


Figure 24 Series of micrographs showing motion of dislocations along slip traces in an aged specimen during in-situ deformation in HVEM. Specimen aged at 623 K for 60 minutes.

this study. During fracture, microcracks were formed in front of the propagating macrocrack. In general, these microcracks increased in size and connected up with the tip of the opening macrocrack. The most important characteristic of these microcracks is their crystallographic character. As they grew in width, they assumed the shape of parallelograms with their edges parallel to the two  $[110]$  directions. This phenomenon can be observed in the micrographs of Figure 25. A schematic illustration of the crack formation is presented in Figure 26. Slip in intersecting slip planes aided the enlargement of the parallelogram-shaped voids.

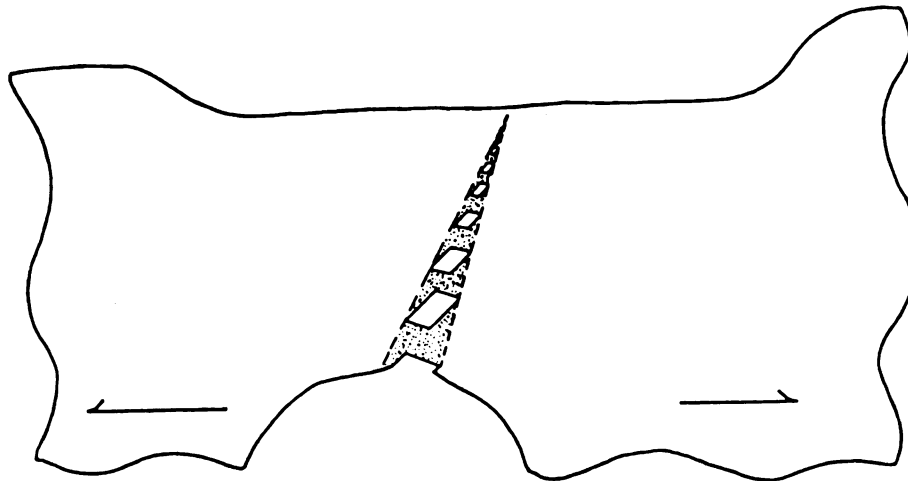


(a)

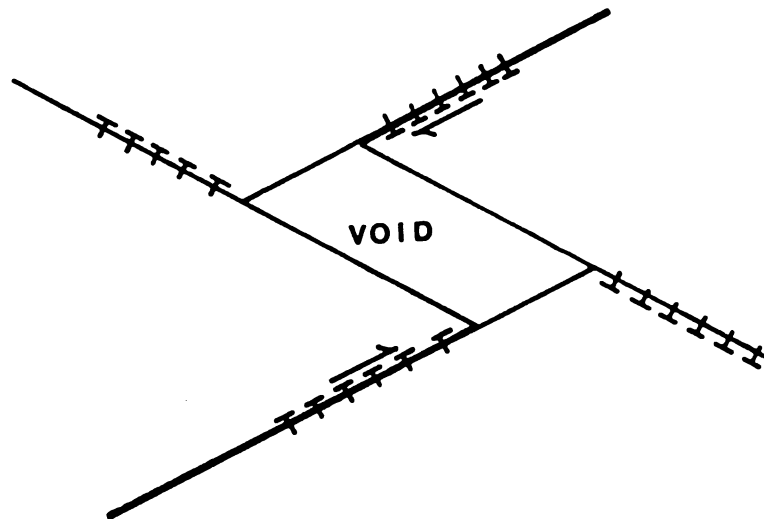


(b)

Figure 25 Typical features of an opening crack in a specimen during in-situ deformation in HVEM.



(a)



(b)

**Figure 26** Schematic representation of (a) the parallelogram-shaped voids of an opening crack, and (b) the arrangement of the dislocations near the shearing edges producing parallelogram-shaped voids.

#### 4.2 Character Analysis of Dislocations that Were Mobile During In-situ Straining

As mentioned in the experimental procedures, two parameters are needed to determine the character of those dislocations that have moved during in-situ deformation. These two parameters are the Burgers vector of the dislocation and the orientation of the dislocation line. The first parameter can be determined by using the " $\vec{g} \cdot \vec{b} = 0$ " criterion and the second parameter can be determined with the help of stereographic projection.

Due to the unavoidable surface effect of the thin foil specimen and the possible inhomogeneity of composition distribution, dislocations were always observed as straight lines with slightly curved ends in the slip traces when the external applied stress was stopped and dislocations were allowed to relax for sufficient length of time. Therefore, the predominant orientation of the dislocation lines was considered for determining the character of the dislocations.

In this thesis, 19 analyses are presented as a representative sampling of the deformation structure in as-quenched and aged specimens. Micrographs which were taken with different reflecting vectors on each set of

dislocations in these analyses are shown from Figure 27 to Figure 45. Tensile axis is marked as "T.A." on these micrographs. Diffraction pattern with two-beam condition, the specimen foil normal and the reflecting vector,  $\vec{g}$ , are also given on these micrographs. Five analyses (#1 - #5) are shown for homogenized specimens. For the specimens with the modulated structure, four analyses (#6 - #9) are given for specimens aged for 20 minutes, four (#10 - #13) for those aged for 40 minutes and six (#14 - #19) for those aged for 60 minutes. All the above analyses are for specimens aged at 623 K. Detailed procedure for carrying out these analyses has already be explained in Chapter 3.

#### 4.2.1 As-quenched specimens

##### Analysis #1:

Dislocations in traces A and B were analyzed with the micrographs shown in Figure 27. These dislocations have been observed to move during in-situ deformation. Set of three micrographs with different  $\vec{g}$  vectors were obtained with different tilting conditions. Possible Burgers vector of these dislocations can be determined by using the following table where "x" represents cases for which the " $\vec{g} \cdot \vec{b} = 0$ " criterion is satisfied, and "-" represents cases for which the " $\vec{g} \cdot \vec{b} = 0$ " criterion is not satisfied.



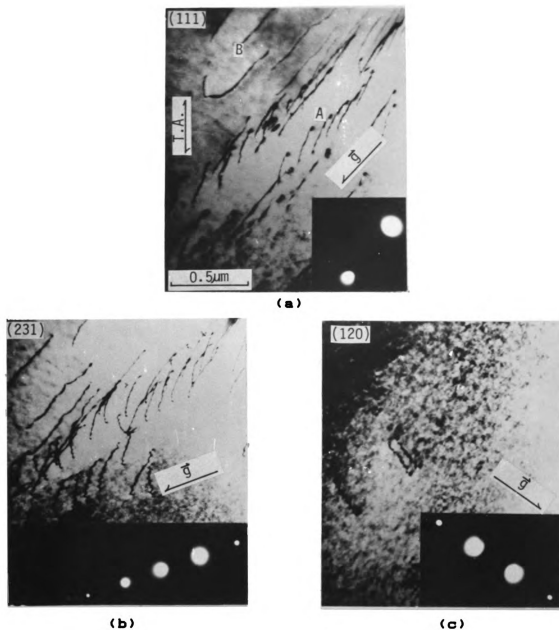


**Figure 27** Burgers vector analysis of dislocations in slip trace A and B of a homogenized specimen during *in-situ* straining in HVEM.

$$(a) \vec{g} = [2\bar{2}0]$$

$$(b) \vec{g} = [\bar{1}1\bar{1}]$$

$$(c) \vec{g} = [00\bar{2}]$$

Figure Number	$\vec{g}$	Possible Burgers Vector					
		$[110]$	$[1\bar{1}0]$	$[101]$	$[10\bar{1}]$	$[011]$	$[01\bar{1}]$
27(a)	$[2\bar{2}0]$	x	-	-	-	-	-
27(b)	$[\bar{1}1\bar{1}]$	x	-	-	x	x	-
27(c)	$[00\bar{2}]$	x	x	-	-	-	-

Since dislocations are out of contrast only in Figure 27(c), Burgers vector of these dislocations is  $[1\bar{1}0]$ . With the help of the  $(111)$  standard stereographic projection, dislocation trace analysis was made as shown in the following table. Particular slip planes that are "Not Possible" are indicated by "NP" in this table.

Slip Trace	Burgers Vector	Slip Plane	Dislocation Line Direction	Dislocation Character
A	$[1\bar{1}0]$	$(111)$ - NP		
		$(11\bar{1})$	$[1\bar{1}0]$	Screw
B	$[1\bar{1}0]$	$(111)$ - NP		
		$(11\bar{1})$	$[011]$	Mixed

Trace analysis indicates that dislocations in trace A are of screw character and in trace B are of mixed character.

#### Analysis #2:

Dislocations in Traces C and D were analyzed with the micrographs shown in Figure 28. Set of four micrographs

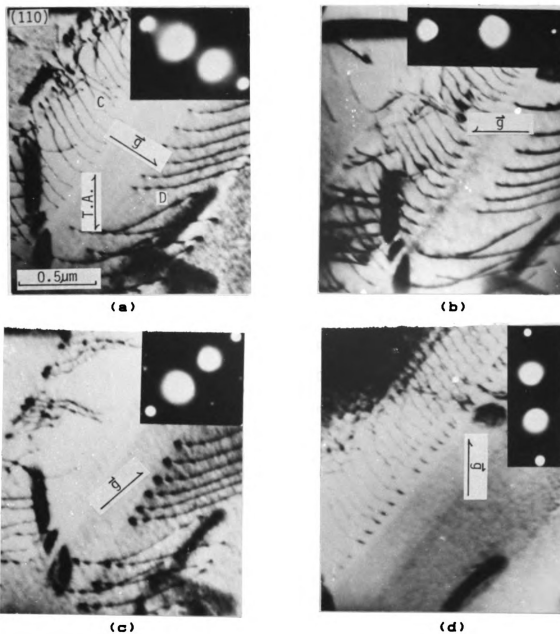


Figure 28 Burgers vector analysis of dislocations in slip trace C and D of a homogenized specimen during in-situ straining in HVEM.

were obtained with different tilting conditions. Possible Burgers vectors of these dislocations can be determined from the following table.

Figure Number	$\vec{g}$	Possible Burgers Vector					
		$[110]$	$[1\bar{1}0]$	$[101]$	$[10\bar{1}]$	$[011]$	$[01\bar{1}]$
28(a)	$[\bar{1}1\bar{1}]$	x	-	-	x	x	-
28(b)	$[\bar{2}20]$	x	-	-	-	-	-
28(c)	$[\bar{1}11]$	x	-	x	-	-	x
28(d)	$[00\bar{2}]$	x	x	-	-	-	-

Dislocations in trace C are out of contrast in Figure 28(c) and dislocations in trace D are out of contrast in Figure 28(d). Therefore possible Burgers vectors for dislocations in trace C is  $[101]$  or  $[01\bar{1}]$  and Burgers vector for dislocations in trace D is  $[1\bar{1}0]$ . In this analysis, information obtained from Figure 28 is not sufficient enough to determine the exact Burgers vector of dislocations in trace C. However, the major aim in this analysis is to find out the character of these dislocations and this can be done although the exact Burgers vector cannot be uniquely determined. With the help of  $(110)$  standard stereographic projection, dislocation trace analysis was made as shown in the following table.

Slip Trace	Burgers Vector	Slip Plane	Dislocation Line Direction	Dislocation Character
C	[101]	( $\bar{1}11$ ) - NP		
		(11 $\bar{1}$ )	[101]	Screw
	[01 $\bar{1}$ ]	(111)	[01 $\bar{1}$ ]	Screw
		( $\bar{1}11$ ) - NP		
D	[1 $\bar{1}$ 0]	(111)	[1 $\bar{1}$ 0]	Screw
		(11 $\bar{1}$ )	[1 $\bar{1}$ 0]	Screw

Trace analysis indicates that dislocations in both slip traces , C and D, are of screw character.

### Analysis #3:

Dislocations in traces E and F were analyzed with the micrographs shown in Figure 29. Set of three micrographs were obtained with different tilting conditions. Possible Burgers vectors for these dislocation can be determined from the following table.

Figure Number	$\vec{g}$	Possible Burgers Vector					
		[110]	[1 $\bar{1}$ 0]	[101]	[10 $\bar{1}$ ]	[011]	[01 $\bar{1}$ ]
29(a)	[ $\bar{1}11$ ]	x	-	x	-	-	x
29(b)	[002]	x	x	-	-	-	-
29(c)	[ $\bar{1}1\bar{1}$ ]	x	-	-	x	x	-

Dislocations in trace E are out of contrast in Figure 29(c) and dislocations in trace F are out of contrast in

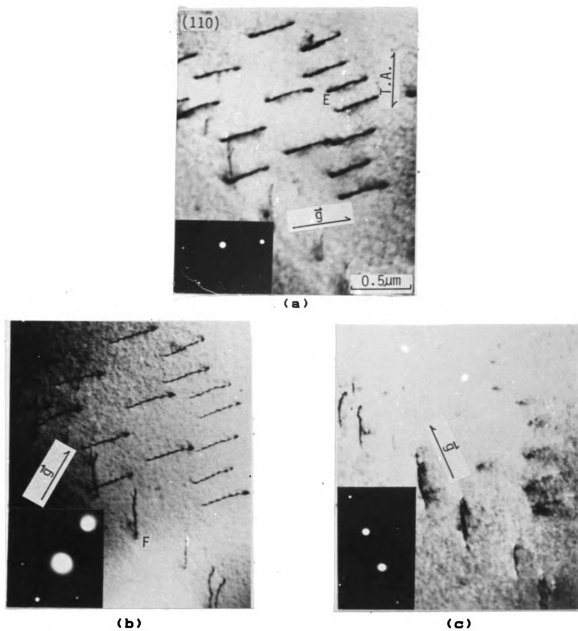


**Figure 29** Burgers vector analysis of dislocations in slip trace E and F of a homogenized specimen during in-situ straining in HVEM.

$$(a) \vec{g} = [\bar{1}11]$$

$$(b) \vec{g} = [002]$$

$$(c) \vec{g} = [\bar{1}\bar{1}\bar{1}]$$

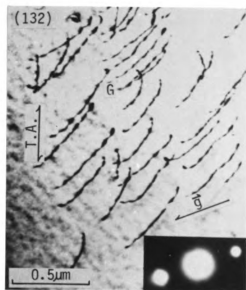
Figure 29(a). Therefore possible Burgers vector for dislocations in trace E is  $[10\bar{1}]$  or  $[011]$  and possible Burgers vector for dislocations in trace F is  $[101]$  or  $[01\bar{1}]$ . With the help of  $(110)$  standard stereographic projection, dislocation trace analysis was made as shown in the following table.

Slip Trace	Burgers Vector	Slip Plane	Dislocation Line Direction	Dislocation Character
E	$[10\bar{1}]$	$(111)$	$[10\bar{1}]$	Screw
		$(111) - NP$		
	$[011]$	$(11\bar{1})$	$[011]$	Screw
		$(1\bar{1}1) - NP$		
F	$[101]$	$(11\bar{1})$	$[101]$	Screw
		$(\bar{1}11) - NP$		
	$[01\bar{1}]$	$(111)$	$[01\bar{1}]$	Screw
		$(\bar{1}11) - NP$		

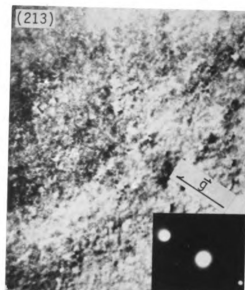
Trace analysis indicates that dislocations in both slip traces , E and F, are of screw character.

#### Analysis #4:

Dislocations in trace G were analyzed with the micrographs shown in Figure 30. Set of two micrographs were obtained with different tilting conditions. Possible Burgers vector can be determined from the following table.



(a)



(b)

Figure 30 Burgers vector analysis of dislocations in slip trace G of a homogenized specimen during in-situ straining in HVEM.

(a)  $\vec{g} = [1\bar{1}1]$

(b)  $\vec{g} = (\bar{1}\bar{1}1)$



Figure Number	$\vec{g}$	Possible Burgers Vector					
		[110]	[1 $\bar{1}$ 0]	[101]	[10 $\bar{1}$ ]	[011]	[01 $\bar{1}$ ]
30(a)	[1 $\bar{1}$ 1]	x	-	-	x	x	-
30(b)	[ $\bar{1}$ 11]	-	x	x	-	x	-

Since dislocations in trace G are out of contrast in Figure 30(b), possible Burgers vector of these dislocations is [1 $\bar{1}$ 0] or [011]. With the help of (110) standard stereographic projection, dislocation trace analysis was made as shown in the following table.

Slip Trace	Burgers Vector	Slip Plane	Dislocation Line Direction	Dislocation Character
G	[1 $\bar{1}$ 0]	(111)	[1 $\bar{1}$ 0]	Screw
		(11 $\bar{1}$ ) - NP		
	[101]	(11 $\bar{1}$ ) - NP		
		( $\bar{1}$ 11) - NP		

Trace analysis indicates that dislocations in trace G are of screw character.

#### Analysis #5:

Dislocations in trace H were analyzed with the micrographs shown in Figure 31. Set of two micrographs were obtained with different tilting conditions. Possible Burgers vector can be determined from the following table.

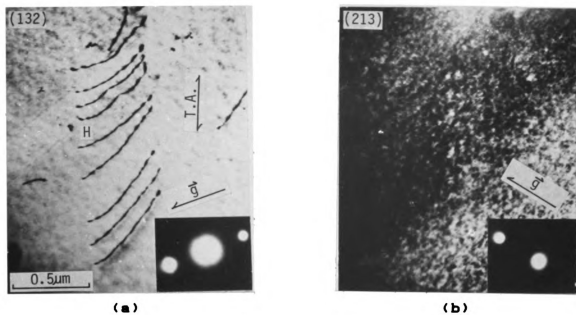


Figure 31 Burgers vector analysis of dislocations in slip trace H of a homogenized specimen during in-situ straining in HVEM.

(a)  $\vec{g} = [1\bar{1}1]$

(b)  $\vec{g} = [\bar{1}1\bar{1}]$

Figure Number	$\vec{g}$	Possible Burgers Vector					
		$[110]$	$[1\bar{1}0]$	$[101]$	$[10\bar{1}]$	$[011]$	$[01\bar{1}]$
31(a)	$[1\bar{1}1]$	x	-	-	x	x	-
31(b)	$[\bar{1}\bar{1}1]$	-	x	x	-	x	-

Since dislocations in trace G are out of contrast in Figure 31(b), possible Burgers vector of these dislocations is  $[1\bar{1}0]$  or  $[011]$ . With the help of  $(110)$  standard stereographic projection, dislocation trace analysis was made as shown in the following table.

Slip Trace	Burgers Vector	Slip Plane	Dislocation Line Direction	Dislocation Character
H	$[1\bar{1}0]$	$(111)$	$[1\bar{1}0]$	Screw
		$(11\bar{1})$ - NP		
	$[101]$	$(11\bar{1})$ - NP		
		$(\bar{1}11)$ - NP		

Trace analysis indicates that dislocations in trace H are of screw character.

### 5.2.2 Specimen aged for 20 minutes

#### Analysis #6:

Dislocations in traces I and J were analyzed with the micrographs shown in Figure 32. Set of four micrographs were obtained with different tilting conditions. Possible Burgers vectors for these dislocations can be determined

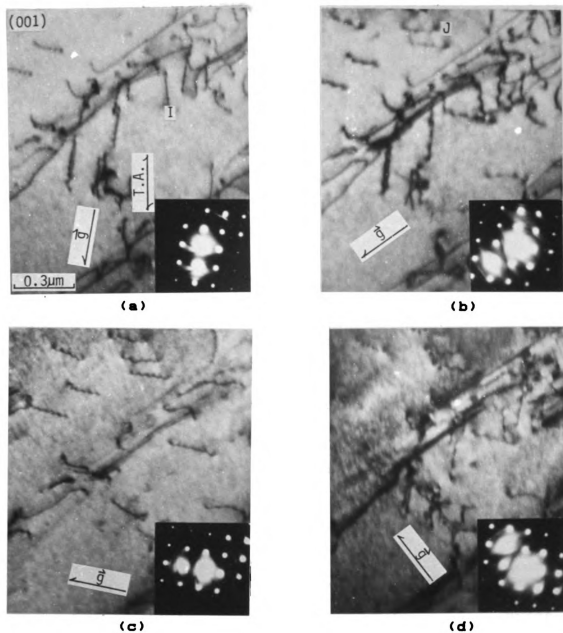


**Figure 32** Burgers vector analysis of dislocations in slip trace I and J of an aged specimen during in-situ straining in HVEM.

Specimen aged at 623 K for 20 minutes.

(a)  $\vec{g} = [200]$

(b)  $\vec{g} = [\bar{2}\bar{2}0]$

(c)  $\vec{g} = [0\bar{2}0]$

(d)  $\vec{g} = [\bar{2}\bar{2}0]$

from the following table.

Figure Number	$\vec{g}$	Possible Burgers Vector					
		$[110]$	$[1\bar{1}0]$	$[101]$	$[10\bar{1}]$	$[011]$	$[01\bar{1}]$
32(a)	$[200]$	-	-	-	-	x	x
32(b)	$[2\bar{2}0]$	x	-	-	-	-	-
32(c)	$[0\bar{2}0]$	-	-	x	x	-	-
32(d)	$[\bar{2}\bar{2}0]$	-	x	-	-	-	-

Dislocations in trace I are out of contrast in Figure 32(c) and dislocations in trace J are out of contrast in Figure 32(a). Therefore possible Burgers vector for dislocations in trace I is  $[101]$  or  $[10\bar{1}]$  and possible Burgers vector for dislocations in trace J is  $[011]$  or  $[01\bar{1}]$ . With the help of  $(110)$  standard stereographic projection, dislocation trace analysis was made as shown in the following table.

Slip Trace	Burgers Vector	Slip Plane	Dislocation Line Direction	Dislocation Character
I	$[101]$	$(11\bar{1})$	$[101]$	Screw
		$(\bar{1}11) - \text{NP}$		
	$[10\bar{1}]$	$(111)$	$[10\bar{1}]$	Screw
		$(1\bar{1}1) - \text{NP}$		
J	$[011]$	$(1\bar{1}1)$	$[011]$	Screw
		$(11\bar{1}) - \text{NP}$		
	$[01\bar{1}]$	$(111)$	$[01\bar{1}]$	Screw
		$(\bar{1}11) - \text{NP}$		

Trace analysis indicates that dislocations in both slip traces , I and J, are of screw character.

**Analysis #7:**

Dislocations in traces K and L were analyzed with the micrographs shown in Figure 33. Set of four micrographs were obtained with different tilting conditions. Possible Burgers vectors for these dislocation can be determined from the following table.

Figure Number	$\vec{g}$	Possible Burgers Vector					
		[110]	[1 $\bar{1}$ 0]	[101]	[10 $\bar{1}$ ]	[011]	[01 $\bar{1}$ ]
33(a)	[ $\bar{1}\bar{1}\bar{1}$ ]	x	-	-	x	x	-
33(b)	[00 $\bar{2}$ ]	x	x	-	-	-	-
33(c)	[2 $\bar{2}$ 0]	x	-	-	-	-	-
33(d)	[ $\bar{1}$ 11]	x	-	x	-	-	x

Dislocations in trace K are out of contrast in Figure 33(b) and dislocations in trace L are out of contrast in Figure 33(c). Therefore Burgers vector for dislocations in trace K is [1 $\bar{1}$ 0] and possible Burgers vector for dislocations in trace L is [10 $\bar{1}$ ] or [011]. With the help of (110) standard stereographic projection, dislocation trace analysis was made as shown in the following table.

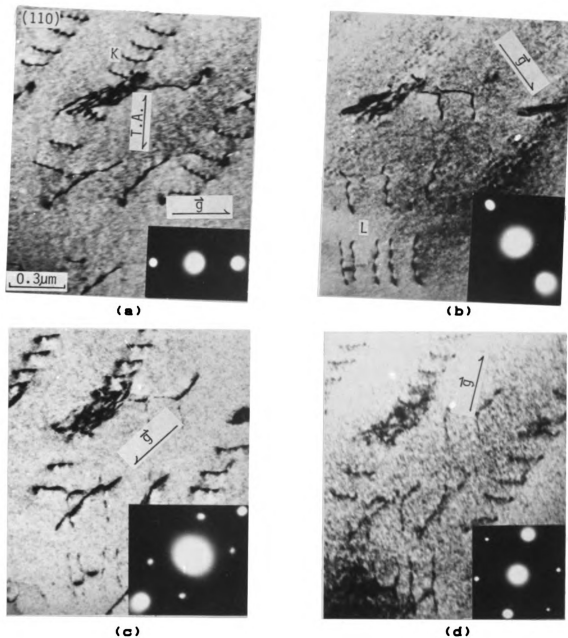


**Figure 33** Burgers vector analysis of dislocations in slip trace K and L of an aged specimen during in-situ straining in HVEM.

Specimen aged at 623 K for 20 minutes.

(a)  $\vec{g} = [111]$

(b)  $\vec{g} = [002]$

(c)  $\vec{g} = [220]$

(d)  $\vec{g} = [\bar{1}11]$

Slip Trace	Burgers Vector	Slip Plane	Dislocation Line Direction	Dislocation Character
K	$[\bar{1}\bar{1}0]$	$(111)$	$[01\bar{1}]$	Mixed
		$(11\bar{1})$	$[101]$	Mixed
L	$[\bar{1}0\bar{1}]$	$(111)$	$[10\bar{1}]$	Screw
		$(1\bar{1}1) - \text{NP}$		
	$[011]$	$(11\bar{1})$	$[011]$	Screw
		$(1\bar{1}1) - \text{NP}$		

Trace analysis indicates that dislocations in trace K are of mixed character and that dislocations in trace L are of screw character.

#### Analysis #8:

Dislocations in traces M and N were analyzed with the micrographs shown in Figure 34. Set of four micrographs were obtained with different tilting conditions. Possible Burgers vectors for these dislocations can be determined from the following table.

Figure Number	$\vec{g}$	Possible Burgers Vector					
		$[110]$	$[\bar{1}\bar{1}0]$	$[101]$	$[10\bar{1}]$	$[011]$	$[01\bar{1}]$
34(a)	$[\bar{1}3\bar{1}]$	-	-	-	x	-	-
34(b)	$[\bar{1}\bar{3}1]$	-	-	x	-	-	-
34(c)	$[\bar{2}00]$	-	-	-	-	x	x
34(d)	$[11\bar{1}]$	-	x	x	-	x	-



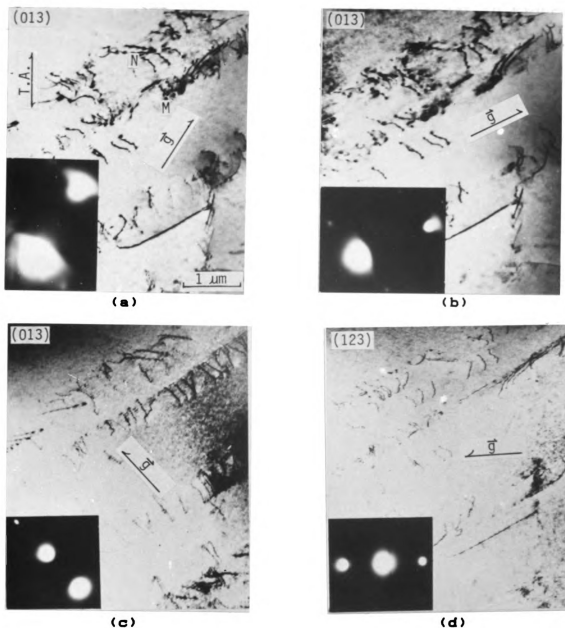


Figure 34 Burgers vector analysis of dislocations in slip trace M and N of an aged specimen during in-situ straining in HVEM.

Specimen aged at 623 K for 20 minutes.

(a)  $\vec{g} = [\bar{1}3\bar{1}]$

(b)  $\vec{g} = [\bar{1}3\bar{1}]$

(c)  $\vec{g} = [\bar{2}00]$

(d)  $\vec{g} = [11\bar{1}]$

Dislocations in trace M are out of contrast in Figures 34(b) and 34(d), and dislocations in trace N are out of contrast in Figure 34(c). Therefore Burgers vector for dislocations in trace M is  $[101]$  and Burgers vector for dislocations in trace N is  $[01\bar{1}]$ . With the help of  $(110)$  standard stereographic projection, dislocation trace analysis was made as shown in the following table.

Slip Trace	Burgers Vector	Slip Plane	Dislocation Line Direction	Dislocation Character
M	$[101]$	$(\bar{1}11)$ $(11\bar{1})$ -NP	$[101]$	Screw
N	$[01\bar{1}]$	$(\bar{1}11)$ $(111)$ - NP	$[0\bar{1}1]$	Screw

Trace analysis indicates that dislocations in both slip traces, M and N, are of screw character.

#### Analysis #9:

Dislocations in traces O were analyzed with the micrographs shown in Figure 35. Set of four micrographs were obtained with different tilting conditions. Possible Burgers vectors for these dislocations can be determined from the following table.

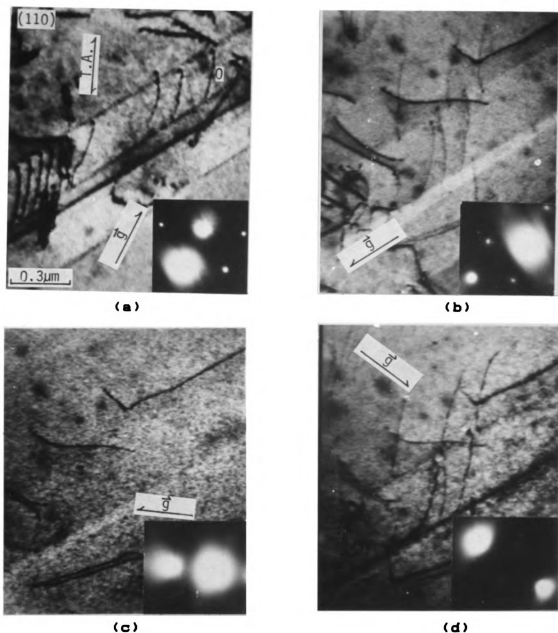


Figure 35 Burgers vector analysis of dislocations in slip trace O of an aged specimen during in-situ straining in HVEM.

Specimen aged at 623 K for 20 minutes.

(a)  $\vec{g} = [\bar{1}11]$

(b)  $\vec{g} = [2\bar{2}0]$

(c)  $\vec{g} = [\bar{1}\bar{1}\bar{1}]$

(d)  $\vec{g} = [\bar{1}\bar{1}\bar{3}]$

Figure Number	$\vec{g}$	Possible Burgers Vector					
		$[110]$	$[1\bar{1}0]$	$[101]$	$[10\bar{1}]$	$[011]$	$[01\bar{1}]$
35(a)	$[\bar{1}11]$	x	-	x	-	-	x
35(b)	$[2\bar{2}0]$	x	-	-	-	-	-
35(c)	$[1\bar{1}1]$	x	-	-	x	x	-
35(d)	$[\bar{1}1\bar{3}]$	x	-	-	-	-	-

Since dislocations in trace O are out of contrast in Figure 35(C), possible Burgers vector for these dislocations is  $[10\bar{1}]$  or  $[011]$ . With the help of  $(110)$  standard stereographic projection, dislocation trace analysis was made as shown in the following table.

Slip Trace	Burgers Vector	Slip Plane	Dislocation Line Direction	Dislocation Character
O	$[10\bar{1}]$	$(111)$	$[10\bar{1}]$	Screw
		$(111) - NP$		
	$[011]$	$(11\bar{1})$	$[011]$	Screw
		$(1\bar{1}1) - NP$		

Trace analysis indicates that dislocations in trace O are of screw character.

#### 4.2.3 Specimen aged for 40 minutes

##### Analysis #10:

Dislocations in trace P were analyzed with the micrographs shown in Figure 36. Set of two micrographs were obtained with different tilting conditions. Possible Burgers vector can be determined from the following table.

Figure Number	$\vec{g}$	Possible Burgers Vector					
		$[110]$	$[1\bar{1}0]$	$[101]$	$[10\bar{1}]$	$[011]$	$[01\bar{1}]$
36(a)	$[1\bar{1}1]$	x	-	-	x	x	-
36(b)	$[\bar{1}11]$	x	-	x	-	-	x

Since dislocations in trace P are not out of contrast in both Figures 36(a) and 36(b), Burgers vector of these dislocations is  $[1\bar{1}0]$ . With the help of  $(110)$  standard stereographic projection, dislocation trace analysis was made as shown in the following table.

Slip Trace	Burgers Vector	Slip Plane	Dislocation Line Direction	Dislocation Character
P	$[1\bar{1}0]$	$(111)$	$[11\bar{2}]$	Edge
		$(11\bar{1})$	$[112]$	Edge

Trace analysis indicates that dislocations in trace P are of edge character.

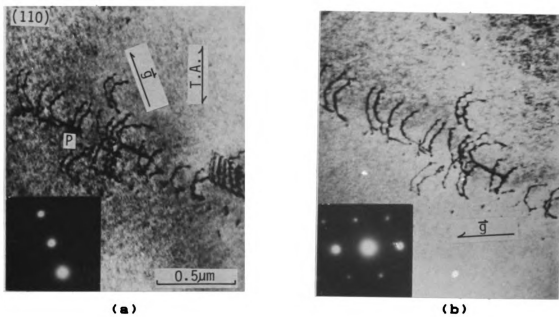


Figure 36 Burgers vector analysis of dislocations in slip trace P of an aged specimen during in-situ straining in HVEM. Specimen aged at 623 K for 40 minutes.

(a)  $\vec{g} = [\bar{1}\bar{1}1]$

(b)  $\vec{g} = [\bar{1}11]$

**Analysis #11:**

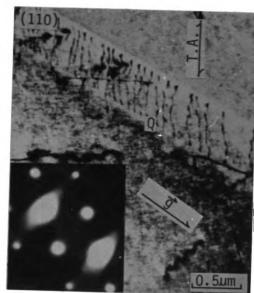
Dislocations in trace Q were analyzed with the micrographs shown in Figure 37. Set of three micrographs were obtained with different tilting conditions. Possible Burgers vectors for these dislocations can be determined from the following table.

Figure Number	$\vec{g}$	Possible Burgers Vector					
		[110]	[ $\bar{1}\bar{1}$ 0]	[101]	[10 $\bar{1}$ ]	[011]	[01 $\bar{1}$ ]
37(a)	[ $\bar{2}$ 20]	x	-	-	-	-	-
37(b)	[11 $\bar{3}$ ]	x	-	-	-	-	-
37(c)	[11 $\bar{1}$ ]	x	-	x	-	-	x

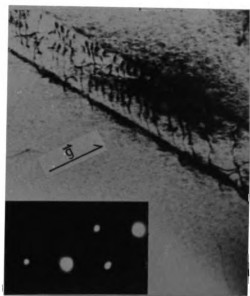
Since dislocations in trace Q are out of contrast in Figure 37(c), possible Burgers vector for these dislocations is [101] or [01 $\bar{1}$ ]. With the help of (110) standard stereographic projection, dislocation trace analysis was made as shown in the following table.

Slip Trace	Burgers Vector	Slip Plane	Dislocation Line Direction	Dislocation Character
Q	[101]	(11 $\bar{1}$ )	[101]	Screw
		( $\bar{1}$ 11) - NP		
	[01 $\bar{1}$ ]	(111)	[01 $\bar{1}$ ]	Screw
		( $\bar{1}$ 11) - NP		

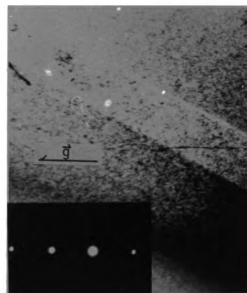
Trace analysis indicates that dislocations in trace Q are of screw character.



(a)



(b)



(c)

Figure 37 Burgers vector analysis of dislocations in slip trace Q of an aged specimen during in-situ straining in HVEM.

Specimen aged at 623 K for 40 minutes.

(a)  $\vec{g} = [\bar{2}20]$

(b)  $\vec{g} = [1\bar{1}\bar{3}]$

(c)  $\vec{g} = [1\bar{1}1]$

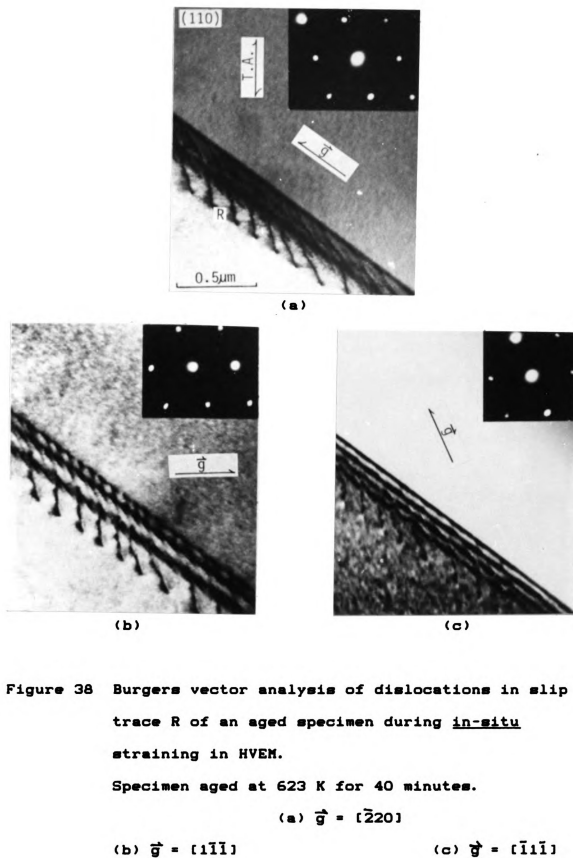


**Analysis #12:**

Dislocations in trace R were analyzed with the micrographs shown in Figure 38. Set of three micrographs were obtained with different tilting conditions. Possible Burgers vectors for these dislocations can be determined from the following table.

Figure Number	$\vec{g}$	Possible Burgers Vector					
		$[110]$	$[1\bar{1}0]$	$[101]$	$[10\bar{1}]$	$[011]$	$[01\bar{1}]$
38(a)	$[\bar{2}20]$	x	-	-	-	-	-
38(b)	$[1\bar{1}\bar{1}]$	x	-	x	-	-	x
38(c)	$[\bar{1}1\bar{1}]$	x	-	-	x	x	-

Since dislocations in trace R are out of contrast in Figure 38(c), possible Burgers vector for these dislocations is  $[10\bar{1}]$  or  $[011]$ . The projected width of the slip trace (dislocation length) on the micrographs will either increase or decrease depending on the sense of tilting. Figure 38(c) was tilted by  $26^\circ$  (counterclockwise about the tensile axis when observed from the bottom of the micrograph) with respect to Figure 38(a) and the width of the slip trace is observed to be less in Figure 38(c). This suggests that the possibility of having  $[10\bar{1}]$  as their Burgers vector can be excluded. With the help of  $(110)$  standard stereographic projection, dislocation trace analysis was made as shown in the following table.



Slip Trace	Burgers Vector	Slip Plane	Dislocation Line Direction	Dislocation Character
R	[011]	(11 $\bar{1}$ )	[101]	Mixed
		(1 $\bar{1}$ 1) - NP		

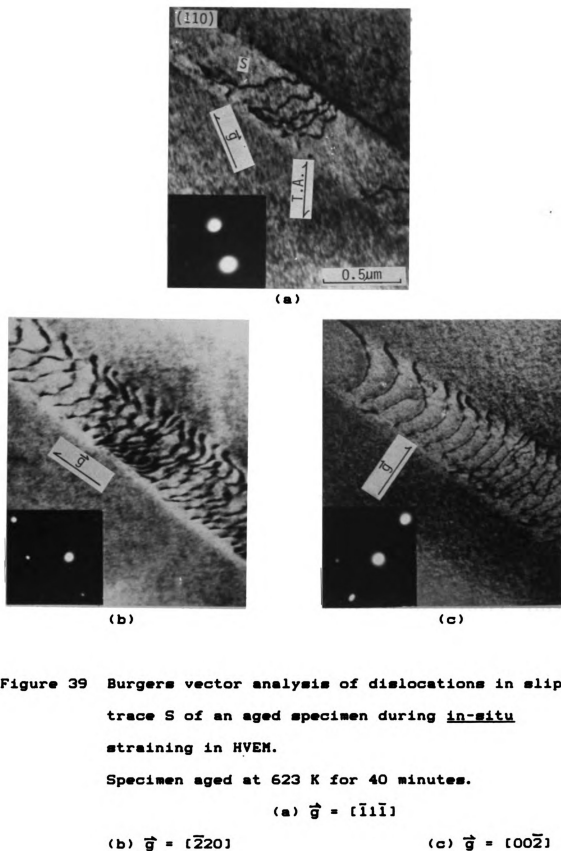
Trace analysis indicates that dislocations in trace R are of mixed character.

#### Analysis #13:

Dislocations in trace S were analyzed with the micrographs shown in Figure 39. Set of three micrographs were obtained with different tilting conditions. Possible Burgers vectors for these dislocations can be determined from the following table.

Figure Number	$\vec{g}$	Possible Burgers Vector					
		[110]	[1 $\bar{1}$ 0]	[101]	[10 $\bar{1}$ ]	[011]	[01 $\bar{1}$ ]
39(a)	[ $\bar{1}$ 1 $\bar{1}$ ]	x	-	-	x	x	-
39(b)	[ $\bar{2}$ 20]	x	-	-	-	-	-
39(c)	[00 $\bar{2}$ ]	x	x	-	-	-	-

Since dislocations in trace S are out of contrast in Figure 39(a), therefore possible Burgers vector for these dislocations is [10 $\bar{1}$ ] or [011]. With the help of (110) standard stereographic projection, dislocation trace analysis was made as shown in the following table.



Slip Trace	Burgers Vector	Slip Plane	Dislocation Line Direction	Dislocation Character
S	$[10\bar{1}]$	$(111)$	$[11\bar{2}]$	Edge
		$(1\bar{1}1)$ - NP		
	$[011]$	$(11\bar{1})$	$[112]$	Edge
		$(1\bar{1}1)$ - NP		

Trace analysis indicates that dislocations in trace S are of edge character.

#### 4.2.4 Specimen aged for 60 minutes

##### Analysis #14:

Dislocations in trace T were analyzed with the micrographs shown in Figure 40. Set of four micrographs were obtained with different tilting conditions. Possible Burgers vectors for these dislocations can be determined from the following table.

Figure Number	$\vec{g}$	Possible Burgers Vector					
		$[110]$	$[1\bar{1}0]$	$[101]$	$[10\bar{1}]$	$[011]$	$[01\bar{1}]$
40(a)	$[1\bar{1}1]$	x	-	-	x	x	-
40(b)	$[002]$	x	x	-	-	-	-
40(c)	$[\bar{2}20]$	x	-	-	-	-	-
40(d)	$[\bar{1}11]$	x	-	x	-	-	x

Since dislocations in trace T are out of contrast in Figure 40(b), Burgers vector for these dislocations is

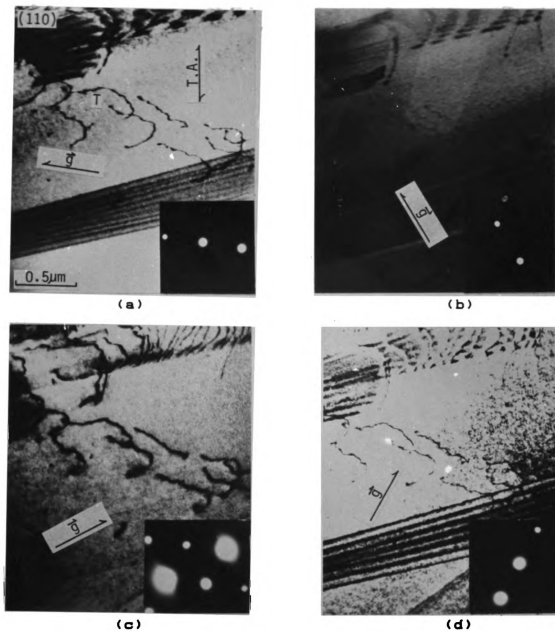


**Figure 40** Burgers vector analysis of dislocations in slip trace T of an aged specimen during in-situ straining in HVEM.

Specimen aged at 623 K for 60 minutes.

(a)  $\vec{g} = [1\bar{1}1]$

(b)  $\vec{g} = [002]$

(c)  $\vec{g} = [\bar{2}20]$

(d)  $\vec{g} = [\bar{1}11]$

$[1\bar{1}0]$ . With the help of  $(110)$  standard stereographic projection, dislocation trace analysis was made as shown in the following table.

Slip Trace	Burgers Vector	Slip Plane	Dislocation Line Direction	Dislocation Character
T	$[1\bar{1}0]$	$(111)$	$[01\bar{1}]$	Mixed
		$(11\bar{1})$	$[101]$	Mixed

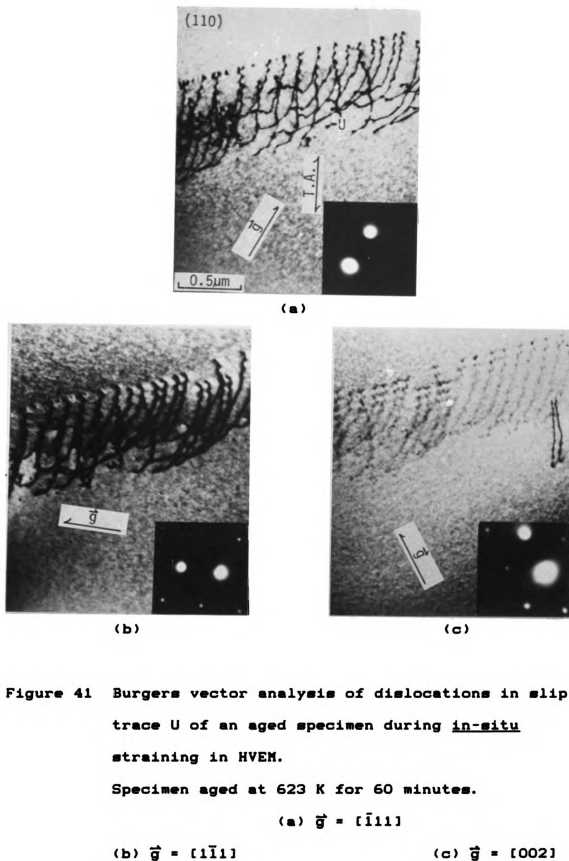
Trace analysis indicates that dislocations in trace T are of mixed character.

#### Analysis #15:

Dislocations in trace U were analyzed with the micrographs shown in Figure 41. Set of three micrographs were obtained with different tilting conditions. Possible Burgers vectors for these dislocation can be determined from the following table.

Figure Number	$\vec{g}$	Possible Burgers Vector					
		$[110]$	$[1\bar{1}0]$	$[101]$	$[10\bar{1}]$	$[011]$	$[01\bar{1}]$
41(a)	$[\bar{1}11]$	x	-	x	-	-	x
41(b)	$[1\bar{1}1]$	x	-	-	x	x	-
41(c)	$[002]$	x	x	-	-	-	-

Since dislocations in trace U are out of contrast in Figure 41(c), Burgers vector for these dislocations is  $[1\bar{1}0]$ . With the help of  $(110)$  standard stereographic





projection, dislocation trace analysis was made as shown in the following table.

Slip Trace	Burgers Vector	Slip Plane	Dislocation Orientation	Dislocation Character
U	$[\bar{1}\bar{1}0]$	$(111)$	$[10\bar{1}]$	Mixed
		$(11\bar{1})$	$[011]$	Mixed

Trace analysis indicates that dislocations in trace U are of mixed character.

#### Analysis #16:

Dislocations in trace V were analyzed with the micrographs shown in Figure 42. Set of three micrographs were obtained with different tilting conditions. Possible Burgers vectors for these dislocations can be determined from the following table.

Figure Number	$\vec{g}$	Possible Burgers Vector					
		$[110]$	$[\bar{1}\bar{1}0]$	$[101]$	$[10\bar{1}]$	$[011]$	$[01\bar{1}]$
42(a)	$[\bar{1}\bar{1}1]$	x	-	x	-	-	x
42(b)	$[\bar{1}\bar{1}\bar{1}]$	x	-	-	x	x	-
42(c)	$[002]$	x	x	-	-	-	-

Since dislocations in trace V are out of contrast in Figure 42(c), Burgers vector for these dislocations is  $[\bar{1}\bar{1}0]$ . With the help of  $(110)$  standard stereographic projection, dislocation trace analysis was made as shown in

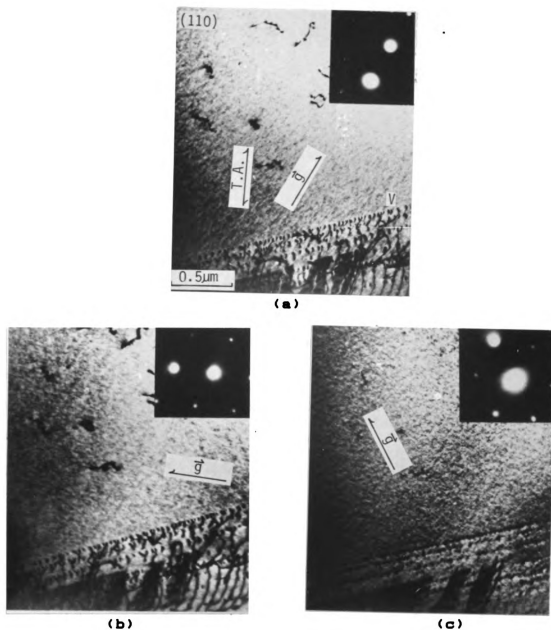


Figure 42 Burgers vector analysis of dislocations in slip trace V of an aged specimen during *in-situ* straining in HVEM. Specimen aged at 623 K for 60 minutes.

(a)  $\vec{g} = [111]$

(b)  $\vec{g} = [111]$

(c)  $\vec{g} = [002]$

the following table.

Slip Trace	Burgers Vector	Slip Plane	Dislocation Line Direction	Dislocation Character
V	$[\bar{1}\bar{1}0]$	(111)	$[10\bar{1}]$	Mixed
		(11 $\bar{1}$ )	$[011]$	Mixed

Trace analysis indicates that dislocations in trace V are of mixed character.

#### Analysis #17:

Dislocations in trace W were analyzed with the micrographs shown in Figure 43. Set of three micrographs were obtained with different tilting conditions. Possible Burgers vectors for these dislocations can be determined from the following table.

Figure Number	$\vec{g}$	Possible Burgers Vector					
		$[110]$	$[\bar{1}\bar{1}0]$	$[101]$	$[10\bar{1}]$	$[011]$	$[01\bar{1}]$
43(a)	$[\bar{1}\bar{1}1]$	x	-	x	-	-	x
43(b)	$[1\bar{1}1]$	x	-	-	x	x	-
43(c)	$[002]$	x	x	-	-	-	-

Since dislocations in trace W are out of contrast in Figure 43(c), Burgers vector for these dislocations is  $[110]$ . With the help of (110) standard stereographic projection, dislocation trace analysis was made as shown in the following table.

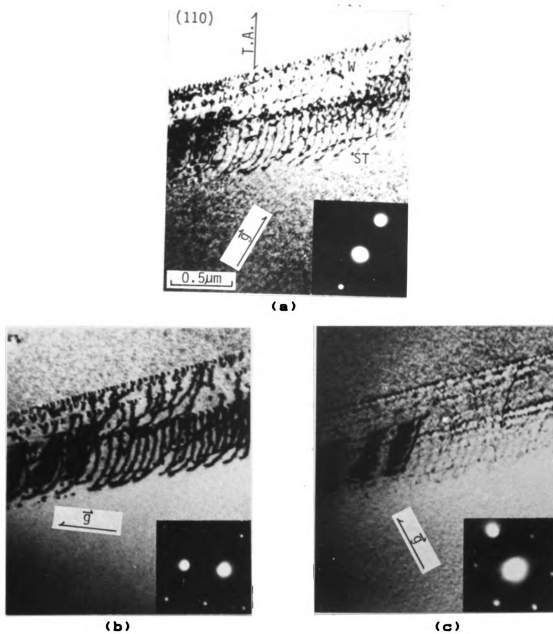


**Figure 43** Burgers vector analysis of dislocations in slip trace W of an aged specimen during in-situ straining in HVEM. Specimen aged at 623 K for 60 minutes.

$$(a) \vec{g} = [\bar{1}11]$$

$$(b) \vec{g} = [1\bar{1}1]$$

$$(c) \vec{g} = [002]$$

Slip Trace	Burgers Vector	Slip Plane	Dislocation Line Direction	Dislocation Character
W	$[\bar{1}\bar{1}0]$	$(111)$	$[10\bar{1}]$	Mixed
		$(11\bar{1})$	$[011]$	Mixed

Trace analysis indicates that dislocations in trace W are of mixed character.

#### Analysis #18:

Dislocations in trace X were analyzed with the micrographs shown in Figure 44. Set of four micrographs were obtained with different tilting conditions. Possible Burgers vectors for these dislocations can be determined from the following table.

Figure Number	$\vec{g}$	Possible Burgers Vector					
		$[110]$	$[\bar{1}\bar{1}0]$	$[101]$	$[10\bar{1}]$	$[011]$	$[01\bar{1}]$
44(a)	$[\bar{1}\bar{1}1]$	x	-	-	x	x	-
44(b)	$[\bar{2}02]$	-	-	x	-	-	-
44(c)	$[\bar{2}20]$	x	-	-	-	-	-
44(d)	$[02\bar{2}]$	-	-	-	-	x	-

Since dislocations in trace X are out of contrast in Figure 44(b), Burgers vector for these dislocations is  $[101]$ . With the help of  $(111)$  standard stereographic projection, dislocation trace analysis was made as shown in the following table.

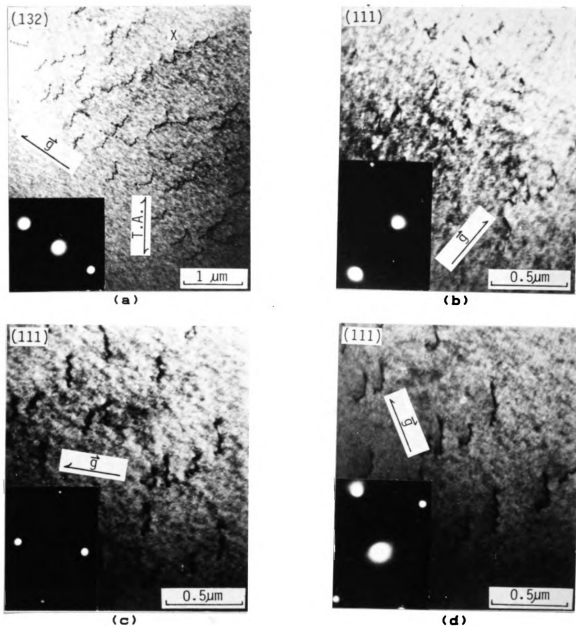


**Figure 44** Burgers vector analysis of dislocations in slip trace X of an aged specimen during in-situ straining in HVEM.

Specimen aged at 623 K for 60 minutes.

(a)  $\vec{g} = [111]$

(b)  $\vec{g} = [\bar{2}02]$

(c)  $\vec{g} = [\bar{2}20]$

(d)  $\vec{g} = [02\bar{2}]$

Slip Trace	Burgers Vector	Slip Plane	Dislocation Line Direction	Dislocation Character
X	$[101]$	$(\bar{1}11)$	$[110]$	Mixed
		$(11\bar{1})$ - NP		

Trace analysis indicates that dislocations in trace X are of mixed character.

#### Analysis #19:

Dislocations with line directions marked Y and Z were analyzed with the micrographs shown in Figure 45. Dislocations with line direction marked Y were observed to reorient into the direction marked Z during in-situ straining. Set of three micrographs were obtained with different tilting conditions. Possible Burgers vectors for these dislocations can be determined from the following table.

Figure Number	$\vec{g}$	Possible Burgers Vector					
		$[110]$	$[1\bar{1}0]$	$[101]$	$[10\bar{1}]$	$[011]$	$[01\bar{1}]$
45(a)	$[\bar{1}1\bar{1}]$	x	-	-	x	x	-
45(b)	$[00\bar{2}]$	x	x	-	-	-	-
45(c)	$[\bar{1}11]$	x	-	x	-	-	x

Since dislocations with line direction marked Y and Z are out of contrast in Figure 45(a), Burgers vector for these dislocations is  $[10\bar{1}]$  or  $[011]$ . With the help of  $(110)$  standard stereographic projection, dislocation trace

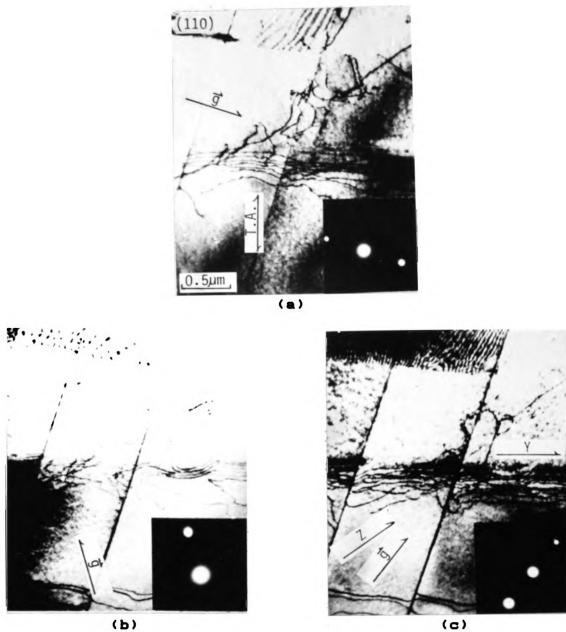


Figure 45 Burgers vector analysis of dislocations that lie along directions marked Y and Z in an aged specimen during in-situ straining in HVEM. Specimen aged at 623 K for 60 minutes.

$$(a) \vec{g} = [\bar{1}1\bar{1}]$$

$$(b) \vec{g} = [00\bar{2}]$$

$$(c) \vec{g} = [\bar{1}11]$$



analysis was made as shown in the following table.

Slip Trace	Burgers Vector	Slip Plane	Dislocation Line Direction	Dislocation Character
Y	[10 $\bar{1}$ ]	(111)	[ $\bar{1}$ 2 $\bar{1}$ ]	Edge
		(1 $\bar{1}$ 1) - NP		
	[011]	(11 $\bar{1}$ )	[2 $\bar{1}$ 1]	Edge
		(1 $\bar{1}$ 1) - NP		
Z	[10 $\bar{1}$ ]	(111)	[ $\bar{1}$ 10]	Mixed
		(1 $\bar{1}$ 1) - NP		
	[011]	(11 $\bar{1}$ )	[ $\bar{1}$ 10]	Mixed
		(1 $\bar{1}$ 1) - NP		

Trace analysis indicates that dislocations with line direction marked Y are of edge character. Some of these dislocations, that have reoriented along Z direction possess mixed character.

Results of all these 19 dislocation character analyses are summarized in Table 2.

**Table 2 Summary of the dislocation character analyses of  
thin foil specimens deformed in-situ.**

<b>Analysis Number</b>	<b>Aging Time (Minutes)</b>	<b>Figure Number</b>	<b>Slip Trace</b>	<b>Dislocation Character</b>
#1	0	27	A B	Screw Mixed
#2	0	28	C D	Screw Screw
#3	0	29	E F	Screw Screw
#4	0	30	G	Screw
#5	0	31	H	Screw
#6	20	32	I J	Screw Screw
#7	20	33	K L	Mixed Screw
#8	20	34	M N	Screw Screw
#9	20	35	O	Screw
#10	40	36	P	Edge
#11	40	37	Q	Screw
#12	40	38	R	Mixed
#13	40	39	S	Edge
#14	60	40	T	Mixed
#15	60	41	U	Mixed
#16	60	42	V	Mixed
#17	60	43	W	Mixed
#18	60	44	X	Mixed
#19	60	45	Y Z	Edge Mixed

## CHAPTER 5

### DISCUSSION

#### 5.1 Theoretical Models

Among all the theories reviewed in Chapter 2, only the theories proposed by Kato et al. [10] and Ardell [11] are considered not to have any major drawbacks. In order to find out which is the most suitable one, detailed discussion of these two theories is presented in this chapter.

Ardell [11] compared the incremental yield stresses calculated with Equation (42) for four Cu-Ni-Fe alloy systems with the values predicted by the equations of Kato et al. and Cahn. Results reproduced from his paper, as shown in Table 3, show that Ardell's predictions give extremely good agreement to the experimental values. The values predicted by the K-M-S theory are much higher than those predicted by Ardell for Cu-Ni-Fe alloys. Parameters of the Cu-Ni-Fe alloy systems used for this calculation are given in Table 4 [11]. If Ardell's equation is a universal

**Table 3 Comparison of the experimental and theoretically predicted values of incremental yield stress of Cu-Ni-Fe alloys. Theoretical values are obtained by using equations derived by Ardell, Cahn, and Kato et al. [11].**

Alloy #	Aging Temp (K)	$\lambda$ (nm)	$A$	$\tau$	Ardell	$\tau$ (NM/m <sup>2</sup> )		KMS
						Cahn Screw	Edge	
1	625	6.1	0.107	23.2	30.1	0.83	28.6	94.7
		8.2	0.115	38.5	41.0	1.28	44.0	101.0
		11.0	0.121	56.2	54.9	1.92	66.0	107.0
		16.3	0.131	61.7	80.6	3.31	113.4	115.3
1	775	15.2	0.090	24.5	41.0	1.46	49.9	79.0
		21.5	0.090	36.3	51.8	2.06	70.4	79.0
		25.9	0.089	42.1	57.5	2.42	83.0	78.3
		44.4	0.095	43.4	91.9	4.73	162.2	83.7
2	625	5.0	0.037	8.2	4.5	0.09	2.9	35.3
		8.2	0.042	19.3	7.8	0.18	6.1	40.3
		7.1	0.052	46.4	10.3	0.24	8.2	50.0
		12.0	0.069	74.5	23.0	0.71	24.3	66.3
3	625	7.0	0.059	14.7	20.8	0.54	18.8	68.3
		7.0	0.091	35.0	42.9	1.30	44.4	105.3
		5.1	0.114	67.6	50.5	1.49	50.8	131.7
		13.5	0.124	79.7	110.1	4.59	157.1	142.3

\* Alloy #1: 51.5Cu-33.5Ni-15.0Fe

Alloy #2: 32.0Cu-45.5Ni-22.5Fe

Alloy #3: 64.0Cu-27.0Ni-9.0Fe

**Table 4** Values of the parameters used in estimating the incremental yield stress in Cu-Ni-Fe alloys [11].  
 $\Gamma$  was calculated from Equation (44) using  
 $\ln(L/r) = 4$ .

Alloy #	$n$	$Y$ (GN/m <sup>2</sup> )	$G$ (GN/m <sup>2</sup> )	$\nu$	Edge	$\Gamma(Gb^2)$ Screw	Mixed
1	0.0130	166.2	45.9	0.394	0.111	0.732	0.267
2	0.0127	186.0	52.0	0.386	0.118	0.718	0.268
3	0.0184	153.3	41.9	0.399	0.107	0.741	0.266

\* Alloy #1: 51.5Cu-33.5Ni-15.0Fe

Alloy #2: 32.0Cu-45.5Ni-22.5Fe

Alloy #3: 64.0Cu-27.0Ni-9.0Fe

equation for spinodal alloys, it should also work for other spinodal alloy systems. In order to check the validity of Ardell's theory, similar calculations were carried out for Cu-10Ni-6Sn spinodal alloy used in this study. This alloy was also used by Kato et al. [10] during their investigations. Parameters of this alloy system used for the calculations are given in Table 5. The incremental yield stresses of this alloy with various aging treatments were calculated by using Equation (42) proposed by Ardell. The values thus obtained were compared with values computed by the equations of Cahn [3] and Kato et al. [10]. Results of this comparison are presented in Table 6. As can be seen in this table, values based on Ardell's equation are about an order of magnitude smaller than the experimental values in the earlier stages of decomposition. However, values based on the theory by Kato et al. are of the same order of magnitude as the experimental values of the incremental yield stress.

It is evident that although the calculated incremental yield stress based on Ardell's model are in excellent agreement with the experimental values for Cu-Ni-Fe, the agreement is not good for Cu-10Ni-6Sn alloy. In order to investigate this discrepancy, the parameters used for the computations presented in Table 4 and Table 5 are compared. The major difference is found to be in the prediction of the line tension of the dislocation,  $\Gamma$ . In Cu-10Ni-6Sn alloy, a

**Table 5** Values of the parameters used in estimating the incremental yield stress in a Cu-10Ni-6Sn alloy aged at 623 K for various lengths of time (in minutes) [45].

Aging Time	A	$\lambda$ (nm)	$n$	$\gamma$ (GN/m <sup>2</sup> )	b (nm)	$\Gamma$ (N)
5	0.005	5.3	0.25	114.8	0.257	$5.0 \times 10^{-9}$
20	0.016	6.8	0.25	114.8	0.257	$5.0 \times 10^{-9}$
60	0.018	8.0	0.25	114.8	0.257	$5.0 \times 10^{-9}$
240	0.024	9.0	0.25	114.8	0.257	$5.0 \times 10^{-9}$
1440	0.030	10.0	0.25	114.8	0.257	$5.0 \times 10^{-9}$

**Table 6 Comparison of the experimental and theoretically predicted values of incremental yield stress of Cu-10Ni-6Sn spinodal alloy aged for various length of time at 623 K.**

Aging Time (Minutes)	Experimental Values (MN/m <sup>2</sup> )	Theoretical Model		
		Cahn	KMS (MN/m <sup>2</sup> )	Ardell
5	30.0	0.1	58.6	2.0
20	110.0	0.5	187.5	16.5
60	140.0	0.8	211.0	22.4
240	180.0	1.6	281.3	39.2
1440	250.0	2.8	351.6	61.0



fixed line tension model was used by Kato et al. [10] and the line tension of the dislocation is assumed to be constant and is written as

$$\Gamma = Gb^2, \quad (43)$$

where "G" is the shear modulus of the alloy. In this case, the character of the dislocation is ignored. In Cu-Ni-Fe alloys, a free line tension model (Devitt-Koehler model) was used by Ardell [11], where  $\Gamma$  depends on the angle  $\theta$  between the dislocation line and its Burgers vector according to the formula [46]

$$\Gamma = \frac{Gb^2}{4\pi} \left[ \frac{1 + \nu - 3\nu \sin^2 \theta}{1 - \nu} \right] \ln\left(\frac{L}{r}\right), \quad (44)$$

where " $\nu$ " is Poisson's ratio and "L" and "r" are the outer and inner cut-off distances, respectively, used in calculating the line energy of the dislocation. In the free line tension model, the orientation of the dislocation is taken into consideration. In this study, the free line tension model is considered to be more accurate than the fixed line tension model. In addition, the parameters used in this calculation for Cu-10Ni-6Sn alloy were obtained from the published data [45] based on the x-ray studies on the same alloy. Since such measurements will smear out local inhomogeneities, potential errors can be present in this data.

For screw, edge and mixed (the kind of mixed dislocation proposed by Kato et al.) dislocations, the angles between the dislocation lines and their Burgers vectors are 0, 90 and 60 degrees respectively. The inner cut-off distance is usually chosen to lie within the range  $b < r < 4b$ . The outer cut-off distance is defined as the distance between two parallel dislocations of opposite signs and it is much more difficult to estimate. However, in this study, it is reasonable to assume this outer cut-off distance to be equal to the foil thickness in the field of view in transmission electron microscopy, which is about  $2000\text{\AA}$ . This value is chosen because these two theories are compared with experimental results of dislocation character obtained from in-situ deformation in HVEM. The line tensions of edge, screw and mixed dislocations calculated by using the free line tension model, with  $\nu = 0.4$  and  $r = 5\text{\AA}$ , are

$$\begin{aligned}\Gamma_e &= 0.159 Gb^2 && \text{for edge dislocations,} \\ \Gamma_s &= 1.112 Gb^2 && \text{for screw dislocations, and} \\ \Gamma_m &= 0.397 Gb^2 && \text{for mixed dislocations.}\end{aligned}\tag{45}$$

For mixed dislocations,  $\Gamma = 0.397 Gb^2$ , which is smaller than  $\Gamma = Gb^2$  as used by Kato et al. [10] in their derivation. Using the shear modulus of copper ( $G = 42.1 \text{ GN/m}^2$ ) and  $b = 2.57\text{\AA}$ , the line tensions can be estimated to be

$$\begin{aligned}
 \Gamma_e &= 4.42 \times 10^{-10} \text{ N}, \\
 \Gamma_s &= 3.09 \times 10^{-9} \text{ N}, \quad \text{and} \\
 \Gamma_m &= 1.10 \times 10^{-9} \text{ N}.
 \end{aligned}
 \tag{46}$$

As has been mentioned in Chapter 2, Cahn [3] as well as Kato et al. [10] solved the force-balance equations, Equations (16) and (35), by assuming that the slope of the dislocation line to be very small, i.e.  $\Delta Y_b / \Gamma \ll 1$ . With this assumption the denominator of the first term of Equations (16) and (35) can be eliminated and the second term can also be simplified. Since  $\Delta Y_b / \Gamma$  is dependent on the estimation of the line tension, recalculation of this parameter was made by using the line tension from Equation (46). For a Cu-10Ni-6Sn alloy aged for 20 minutes at 623 K, it gives

$$\begin{aligned}
 \Delta Y_b / \Gamma_e &= 0.289 \text{ for edge dislocations,} \\
 \Delta Y_b / \Gamma_s &= 0.041 \text{ for screw dislocations, and} \\
 \Delta Y_b / \Gamma_m &= 0.116 \text{ for mixed dislocations,}
 \end{aligned}
 \tag{47}$$

whereas  $\Delta Y_b / \Gamma = 0.026$  with  $\Gamma = 5 \times 10^{-9} \text{ N}$  as calculated from the fixed line tension model by Kato et al. [10]. As can be seen from Equation (47), this parameter is not much less than unity especially for edge dislocations.

In order to find out how this parameter,  $\Delta Y_b / \Gamma$ , can affect the solutions of the force-balance equations, numerical method were used to solve these equations,

Equations (16) and (35), without using any assumptions. Fortunately, numerical values for the critical resolved shear stress, the amplitude of the dislocation and the maximum slope of the dislocation line are not very much different from those obtained by using analytical methods used by Cahn and Kato et al. for screw and mixed dislocations. However, in the case of edge dislocations, especially for those in specimens with longer aging treatment, numerical results show a much larger amplitude and maximum slope than those obtained analytically, as shown in Table 7. Ardell's derivation adapted Cahn's analytical solutions for the amplitude and maximum slope of edge dislocations. In Cahn's derivation, the amplitude and the maximum slope of edge dislocations were assumed to be much less than unity, i.e.,  $\Delta\gamma_b/\Gamma_B \ll 1$ . Therefore, for  $\Delta\gamma_b/\Gamma_B$  not much less than unity, Ardell's prediction of incremental yield stress for edge dislocations is not accurate.

Ardell's prediction that edge dislocations are responsible for the age-hardening in the spinodally modulated structure is also inadequate from the consideration of the free energy of dislocations. Kato et al. [47] have calculated the free energy difference between stable and unstable configurations of screw and mixed dislocations when the external applied stress is absent. Their results are

**Table 7 Comparison of numerically calculated values of amplitude,  $v$ , and maximum slope,  $\theta_c$ , for edge dislocations in Cu-33.5Ni-15.0Fe alloy and values predicted by Cahn's model [3].**

Aging Temp. (K)	$\lambda$ (nm)	$A$	Numerical Solution		Cahn's solution	
			$v$ (nm)	$\theta_c$	$v$ (nm)	$\theta_c$
625	16.3	0.131	64.3	3.03	5.18	0.815

$$\Delta F = \Gamma \left( \frac{\Lambda \gamma b}{\sqrt{3} \Gamma \beta} \right)^2 \quad \text{for screw dislocations,} \quad (48)$$

and

$$\Delta F = \Gamma \left( \frac{\Lambda \gamma b}{\Gamma \beta} \right) \quad \text{for mixed dislocations.} \quad (49)$$

Equation (48) gives a smaller value than Equation (49) with  $\Lambda \gamma b / \Gamma \beta \ll 1$ . This indicates that mixed dislocations face a larger resistance to their motion and are energetically more stable than screw dislocations. Therefore, the motion of these mixed dislocations determines the CRSS of the spinodally modulated structure.

A similar approach can also be made for edge dislocations. The configuration of an edge dislocation with zero external applied stress can be written as

$$x = B_1 + B_2 \sin\left(\frac{\beta y}{\sqrt{6}}\right), \quad (50)$$

with

$$B_1 = \frac{\pi}{\sqrt{2}\beta}, \quad B_2 = \frac{2\sqrt{3}\Lambda \gamma b}{\Gamma \beta^2} \quad \text{for stable configurations,} \quad (51)$$

and

$$B_1 = \frac{\sqrt{2}\pi}{\beta}, \quad B_2 = 0 \quad \text{for unstable configurations.} \quad (52)$$

The free energy per unit length of an edge dislocation in

the absence of applied stress can be written as

$$F_e = \frac{1}{\sqrt{6}\lambda} \int_0^{\frac{\pi}{2}} \left[ \Gamma \left( 1 + \frac{1}{2} \left( \frac{dx}{dy} \right)^2 \right) + \frac{2\Delta\gamma b}{\sqrt{3}\beta} \sin\left(\frac{\beta y}{\sqrt{6}}\right) \cos\left(\frac{\beta x}{\sqrt{2}}\right) \right] dy. \quad (53)$$

Substituting Equation (50), either with Equation (51) or (52), into Equation (53), the free energy corresponding to an edge dislocation can be obtained as

$$F_e = \Gamma \left[ 1 + \frac{(1-\sqrt{2})}{2} \left( \frac{\Delta\gamma b}{\Gamma\beta} \right)^2 \right] \text{ for stable configurations,} \quad (54)$$

and

$$F_e = \Gamma \quad \text{for unstable configurations.} \quad (55)$$

The difference between Equation (54) and (55) is

$$\Delta F = \Gamma \frac{(\sqrt{2} - 1)}{2} \left( \frac{\Delta\gamma b}{\Gamma\beta} \right)^2. \quad (56)$$

Substituting the parameters for the Cu-10Ni-6Sn alloy together with the different values of line tension (for dislocations with different characters) into Equations (48), (49) and (56) gives

$$\begin{aligned}
 \Delta F &= 7.65 \times 10^{-12} \text{ N}, \\
 \Delta F &= 1.73 \times 10^{-12} \text{ N, and} \\
 \Delta F &= 1.28 \times 10^{-10} \text{ N.}
 \end{aligned}
 \tag{57}$$

Equations (57) indicate that mixed dislocations have a larger barrier for dislocation motion and are energetically more stable than dislocations with other characters.



### 5.2 In-situ Deformation in HVEM

The greatest advantage of studies with the HVEM is the increase of the electron penetration depth due to the higher accelerating voltage, so that observations can be made on thicker regions of the specimens. The deformation structure observed in thicker regions of specimens are more representative of that of specimens deformed in bulk. With in-situ techniques, detailed microscopic information on the behavior of dislocations can be obtained during straining. It is very difficult to draw definite conclusions about the deformation process just by conventional electron microscopic observations of the deformed bulk specimens since the observation is only a small part of the overall picture [49]. Therefore, for establishing reliable models on the behavior of dislocations during deformation, dynamical studies in HVEM are required. It also should be noted that conventional TEM studies on specimens deformed in bulk have several drawbacks. Firstly, it is not certain that the dislocations analyzed have moved during deformation. Secondly, the possibility of dislocations reorienting during foil preparation also exists in such specimens. Thirdly, the dislocations analyzed by conventional TEM could have moved a large distance from the sources emanating them. The interaction of the dislocations with the matrix during their motion could have significantly altered their character.

The major limitations of the HVEM in-situ straining studies are the electron-radiation effects and the surface effects [50]. As regards to the first, energetic electron beams can produce damages by ejecting atoms from their normal lattice positions. This displacement damage has a serious effect on all the structure sensitive properties, of which the mechanical properties are a good example. The interstitial atoms and vacant lattice sites caused by the displacement damage are produced when a lattice atom receives energy more than its displacement energy,  $E_d$ , from the colliding electron.  $E_d$  depends on the material, and the crystal orientation with respect to the direction of the incident electron beam and has been shown to be  $\sim 19$  eV in copper [51]. This displacement energy can be produced by electrons with energies greater than 400 KeV [51]. This effect is particularly important in in-situ straining experiments when extended observations are made to observe the changes during straining of the specimens. In order to minimize the radiation effects, through out this study, HVEM was operated with an accelerating voltage of 400 KV, which is below the critical voltage for copper.

Surface effects are mainly of two kinds [48, 50]; a pinning effect on the moving dislocations due to the surface layer and an image force which usually attracts the dislocations towards the free surface. In thin foils, the

line tension may counterbalance the effect due to the image force [50]. If the forces caused by these surface effects can be in principle handled quantitatively, their calculation in practical cases is intricated [50]. In addition, there remain large uncertainties due to the lack of knowledge of the surface quality (real free surface, contamination layer, oxidation layer), and of the surface effects under dynamical conditions [50, 52]. As mentioned by Fujita et al. [53], the critical foil thickness sufficient to observe the same dynamic behavior as in bulk specimens is about  $2\mu\text{m}$  for copper. Although the regions studied in HVEM during this investigation may be much thinner than this, the surface effects can be assumed to be approximately same in all the specimens. As a result, all the in-situ observations were assumed to be affected by similar surface effects.

A schematic feasibility diagram has been proposed by Martin and Kubin [50] to counter the limitations in in-situ deformation in HVEM. This diagram suggests that, for a typical FCC metal, in-situ experiments should be carried out at high temperatures and at high accelerating voltages so as to be representative of bulk specimens. From the conclusion drawn by Martin and Kubin [50], it is clear that the surface effects were unavoidable in the present study.

Another impediment in in-situ deformation arises from the

difficulty of preparing long specimens with uniform geometry transparent to electrons in the HVEM without mechanical damage [54]. Therefore, the local stress state in the region of observation cannot be determined even if the external applied tensile load is known. Usually, bending stresses that can develop in small transparent thin regions interfere with the applied tensile stress and cause the activation of slip systems that may not have the highest Schmid factor with respect to the particular tensile axis [54]. It is also uncertain whether the first dislocation movement can represent the macroscopic yielding of the specimen. In experiments on the multiplication of dislocations in aluminum, Fujita and Yamada [55] indicated that all the dislocation activities were observed at a stress lower than the apparent yield stress. Therefore, specific checks are necessary to prove that the data obtained from in-situ deformation are relevant for extrapolation to the bulk specimens [50, 54]. It can also be noticed that in most cases the dislocations tend to move cooperatively in groups on a few relatively closely spaced slip planes rather than individually, and independently of each other. This indicates that a triggered action of a few adjacent dislocation sources exists in specimens during in-situ straining [54]. As a result, the in-situ straining observations can be used mainly to understand the detailed of the motion of dislocations in a given lattice, rather than to obtain the characteristics of the dislocation

source.

Results of the dislocation character analysis obtained from the in-situ study indicate that the equilibrium configuration under stress of dislocations that were mobile during deformation in homogenized specimens with shorter aging treatments (20 minutes) are of screw character and in specimens with longer aging treatments (60 minutes) are of mixed character. A transition in the dislocation character, from screw to mixed, occurred in specimens aged for about 40 minutes. This suggests that the theoretical model proposed by Kato et al. [10] may be applicable for specimens that have undergone longer aging treatments.

A parallel study [56] on the same alloy has been carried out by deforming the specimens in bulk and by studying the deformation structure with conventional TEM operated at 100 KV. Comparison between these two studies has been made to check whether the results obtained from in-situ study (termed thin-foils in this section) are relevant to that obtained from the conventional TEM study (termed bulk specimens in this section). Unfortunately, some differences can be noticed especially for homogenized specimens and specimens with shorter aging treatments. In bulk specimens, Shekhar [56] found that the relaxed configuration without stress of dislocations along potentially active slip planes in homogenized specimens are mostly of edge character. In

specimens with shorter aging treatments (5, 20, 40 minutes), dislocations do not have any specific character. Most of these dislocations present in individual slip planes possessed varying mixed characters. There appears to be a tendency for these dislocations to reorient into the  $60^\circ$  mixed orientation (with Burgers vector  $60^\circ$  to the dislocation line direction). However, dislocations along potentially active slip planes in specimens with longer aging treatment (60 minutes), are of a  $60^\circ$  mixed character.

Results of the dislocation analyses in the in-situ study show that mobile dislocations in homogenized thin-foils are mostly of screw character. However, results of the analyses on homogenized bulk specimens indicate that dislocations with character closer to edge were observed along slip traces that were potentially active. Possible explanation for this difference is as follows. Depending on the mobility of the dislocations and its variation with dislocation character, the shape of the dislocation loop produced from a dislocation source may be quite different [57 - 59]. In FCC alloys, the lattice friction on edge dislocations exceeds that on screw dislocations [54, 57 - 59]. This effect will elongate the dislocation loops in the direction perpendicular to the Burgers vector [57, 58], and the operation of a Frank-Read source is controlled by overcoming the lattice friction experienced by edge dislocations. Such an elongated loop will possess larger

segments that will be predominantly of edge character rather than the screw character [57, 59]. Therefore, the possibility of observing dislocations with orientation closer to edge in homogenized bulk specimens is higher than that of dislocations with other characters. Similar observations have been reported on FCC alloys such as Cu-Al [57, 58] and Cu-Zn [59]. Another possible reason for observing dislocations of predominantly edge character in bulk specimens may be due to the possibility that the screw components escaped from the surfaces during foil preparation [60].

Extensive reorientation of dislocations was observed during in-situ straining. However, the mobile dislocations were observed to be predominantly of screw character in their equilibrium configuration under stress. This may be explained on the following basis: The self energy of screw dislocations is much lower than that of edge dislocations and during in-situ straining of thin-foils, the two surfaces are very close to each other. As a result, the dislocations can reorient into screw configuration. Besides, the thin-foil specimens used during in-situ straining are too thin for the Frank-Read sources to operate [57]. As mentioned in the in-situ deformation studies of Molybdenum by Vesely [61, 62], the activity of a dislocation source depends on the orientation of dislocation Burgers vector to the foil surface, and the most active sources are those

which can lose dislocations with lower mobility through the surfaces and leave the ones with higher mobility to propagate through the foil. In homogenized Cu-10Ni-6Sn, an FCC alloy, the mobility of screw dislocations is higher than that of edge dislocations [54]. Therefore, the relaxed configuration under stress of dislocations that were mobile during deformation observed in thin-foils predominantly possessed screw character. The extensive reorientation of dislocations during in-situ straining may be due to the surface effects and the inhomogeneity of the matrix.

Shekhar's study [56] shows that in bulk specimens with shorter aging treatments, dislocations along slip traces do not possess any specific character. However, in this study, results in the thin-foils with shorter aging treatments show a significant disagreement with the bulk specimens. In thin-foils aged for 20 minutes, equilibrium configuration under stress of dislocations that were mobile during deformation were observed to be predominately of screw character. This difference can be explained as follows. In specimens with shorter aging treatments, the resistance by the internal stress field due to the modulated structure may tend to reorient dislocations into mixed character. At this stage of decomposition, the effects due to the local inhomogeneity of the solid solution and the local inhomogeneity of spinodal decomposition are comparable with the effect due to composition modulation. As a result, the



dislocations do not have any specific character in bulk specimens. If an average direction can be assigned for these dislocations, there appears to be a tendency for this average direction to be about  $60^\circ$  to the Burgers vector. This suggests that the modulated structure tends to reorient dislocations into  $60^\circ$  mixed character but is not strong enough to overcome the local inhomogeneities. However, in thin-foils, the effects due to the composition modulation are countered not only by the local inhomogeneities but also by the surface effects. The effects due to the local inhomogeneities in thin-foils will be less significant as compared to that in bulk specimens. In bulk specimens, inhomogeneities present in different regions can affect the shape of the individual dislocation loops by creating drag at different segments of the same loop. This possibility is much less in thin-foils. Therefore, dislocations will attempt to reorient themselves during their motion into a  $60^\circ$  mixed character if the modulation effects dominate the surface effects or stay in screw character otherwise. If modulation effects dominate, such reoriented dislocation will retain their character even in equilibrium state under stress. In this study, the modulation effects in thin-foils aged upto 40 minutes are apparently not strong enough to overcome the surface effects. However, in thin-foils aged for 60 minutes the modulation effects are strong enough to overcome the surface effects. As a result, the dislocations that were mobile during in-situ deformation of such

specimens retained the  $60^\circ$  mixed character even in their equilibrium configuration under stress. In addition, in such specimens, the mobile dislocations were observed to be relatively straight; during their motion, extensive change of character was not observed.

For thin-foils aged for 20 minutes, as mentioned in the general observations, leading dislocations were observed to move in a jerky fashion while the following dislocations were moving relatively smooth. As suggested in the paper by Mori and Kato [44], the motion of glide dislocations in spinodally modulated structure can be activated by the formation of double-kinks. This double-kink formation process may explain the behavior of the leading dislocations. During the motion of dislocations, part of the dislocation may move forward along slip trace to nucleate a double-kink and the kinks expand and reach the ends of the dislocation segment. Hence the motion of these dislocations is seen to be jerky or discontinuous due to the mechanism of accumulated double-kink formation. This double-kink formation process can also be used to explain the jerky motion of mobile dislocations in thin-foils aged for 40 and 60 minutes.

In aged thin-foils, the leading dislocations always moved in a jumpy fashion. However, the following dislocations moved in a relatively smooth fashion until they caught up

with the leading dislocations, which appeared to be facing some kind of a barrier to their motion at a position farther along the slip trace. This behavior may be explained in the following manner. The leading dislocations in each slip trace faces the maximum resistance due to the modulation and localized inhomogeneities. The pile-up stress due to the trailing dislocations appear to aid the leading dislocation to overcome this barrier. Leading dislocation, during its jump, reaches a location where the pile-up stress due to trailing dislocations is no longer effective. It is believed that the motion of dislocations tends to soften the slip traces. This phenomenon has been reported by Clement et al. [63 - 65] in Ni-Cr alloy. Because of this softening process by the leading dislocations, following dislocations experienced a lower resistance than the leading dislocations. Therefore, these following dislocations were observed to move relatively smooth. Since the passage of the leading dislocation tends to soften the path for the trailing dislocations, the process tends to repeat itself so as to cause the jumpy motion to continue. However, in specimens aged for 60 minutes, resistance due to the spinodal modulation are so strong that the influence of the localized softening was not observed.

As has been discussed in Section 5.1, the age-hardening in spinodally modulated structures has been explained on

the basis of an ideal microstructure and dislocations of specific characters in different theories [3, 10, 11]. However, actual experimental observations in a spinodal alloy (Cu-10Ni-6Sn) indicate that factors such as local inhomogeneities play a significant role. These inhomogeneities tend to affect the character of mobile dislocations in specimens that have undergone the earlier stages of decomposition. Theories that attempt to address real materials should take these factors into account.

## CHAPTER 6

### CONCLUSIONS

1. Dislocations do not move as straight lines during in-situ straining studies in HVEM. Extensive reorientation of long dislocation lines occurs continuously during straining of specimens that were homogenized or that have undergone early stages of spinodal decomposition.
2. Motion of dislocation in homogenized structure was observed to be smooth and continuous. On the other hand, motion of dislocation in the modulated structure was jerky.
3. Leading dislocation in each slip trace appears to experience the maximum resistance from the modulated structure, since it stops for sufficient lengths of time between its fast (jumpy) motion. Motion of other dislocations in the slip trace is relatively smooth compared to the leading dislocations.

4. Relaxed configuration under stress of dislocations that were mobile during in-situ straining of homogenized specimens was mainly screw in character.
5. Burgers vector of dislocations that have attained their equilibrium configuration under stress during in-situ deformation of Cu-10Ni-6Sn alloy was analyzed. Dislocations with screw character were observed in specimens aged upto 40 minutes at 623 K. These results indicate that surfaces of the thin foils used in in-situ deformation play an important role with respect to the motion of the dislocations. On the other hand, mixed dislocations, with their Burgers vector at  $60^\circ$  to the dislocation line, play a significant role during deformation of specimens aged for 60 minutes at 623 K.
6. The leading dislocation in specimens with shorter aging treatments (20 minutes), and all the dislocations in specimens with longer aging treatments (40 and 60 minutes) were observed to move in a jerky fashion during in-situ straining. This behavior may be due to the mechanism of double-kink formation, where double-kinks nucleate and subsequently spread to the ends of the dislocations.
7. In specimens aged for 20 minutes, a softening of the slip plane occurs through the movement of the leading

dislocations; the following dislocations move relatively smoother.

8. Comparison of the results from the in-situ straining with the results from specimens deformed in bulk [56] indicates that theories attempting to address real materials should take the local inhomogeneities in the solid solution and the composition modulation due to spinodal decomposition into consideration.
9. Comparison of various theories and the experimental results indicates that the theory proposed by Kato et al. [10] may be the most suitable one to explain the age hardening mechanism of spinodal alloys with an ideal microstructure.

## REFERENCES

1. Hilliard, J. E., Phase Transformation, Aaronson, H. I. ed., American Society of Metals, Metal Park, OH, 1970, p.497.
2. Ditchek, B. and Schwartz, L. H., Annual Review of Materials Science, 9, 219 (1979).
3. Cahn, J. W., "Hardening by spinodal decomposition", Acta Metallurgica, 11, 1275 (1963).
4. Dahlgren, S. D., Ph. D. Thesis, University of California, Berkley, CA, 1966.
5. Dahlgren, S. D., "Correlation of yield strength with internal coherency stress in age-hardened Cu-Ni-Fe alloys", Metallurgical Transactions, 8A, 347 (1977).
6. Carpenter, R. W., "Deformation and fracture of gold-platinum polycrystals strengthened by spinodal decomposition", Acta Metallurgica, 15, 1297 (1967).
7. Ghista, D. N. and Nix, W. D., "A dislocation model pertaining to the strength of elastically inhomogeneous materials", Materials Science and Engineering, 3, 293 (1969).
8. Ditchek, B. and Schwartz, L. H., Proceeding of the 4th International Conference on Strength of Metals and Alloys, 3, 1319 (1976).
9. Hanai, Y., Miyazaki, T. and Mori, H., "Theoretical estimation of the effect of interfacial energy on the mechanical strength of spinodally decomposed alloys", Journal of Materials Science, 14, 599 (1979).
10. Kato, M., Mori, T. and Schwartz, L. H., "Hardening by spinodal modulated structure", Acta Metallurgica, 28, 285 (1980).
11. Ardell, A. J., "Precipitation Hardening", Metallurgical Transactions A, in press.
12. Gibbs, J. W., The Scientific Paper by J. W. Gibbs, Dover, 1961, p.43. (cited in ref. 1)



13. van der Waals, J. D., Z. Phys. Chem, 5, 133 (1890).  
(cited in ref. 1)
14. Daniel, V. and Lipson, H., "An x-ray study of the dissociation of an alloy of copper, iron and nickel", Proceedings of the Royal Society (London), Serial A, 181, 368 (1943).
15. Daniel, V. and Lipson, H., "Dissociation of alloy of copper, iron and nickel further x-ray work", Proceedings of the Royal Society (London), Serial A, 182, 378 (1944).
16. Hillert, M., "A solid-solution model for inhomogeneous system", Acta Metallurgica, 9, 525 (1961).
17. Hillert, M., D. Sc. Thesis, Massachusetts Institute of Technology, MA, 1956.
18. Hillert, M., Cohen, M. and Averbach, B. L., "Formation of modulated structures in Copper-Nickel-Iron alloys", Acta Metallurgica, 9, 536 (1961).
19. Cahn, J. W., "On spinodal decomposition", Acta Metallurgica, 9, 795 (1961).
20. Cahn, J. W., "On spinodal decomposition in cubic crystals", Acta Metallurgica, 10, 179 (1962).
21. Hoffman, D. W., "The effect of atomic misfit on the coexistence and spinodal transformation boundaries in binary alloys", Acta Metallurgica, 26, 933 (1978).
22. Cahn, J. W., "Spinodal decomposition", Trans. AIME, 242, 166 (1968).
23. Soffa, W. A. and Laughlin, D. E., "Recent experimental studies of continuous transformations in alloys: an overview", Proceeding of an International Conference on Solid-solid Phase Transformation, Aaronson, H. I., Laughlin, D. E., Sekerka, R. F. and Wayman, C. M. eds., The Metallurgical Society of AIME, 1982, p.159.
24. Butler, E. P. and Thomas, G., "Structure and properties of spinodally decomposed Cu-Ni-Fe alloys", Acta Metallurgica, 18, 347 (1970).
25. Douglass, D. L. and Barbee, T. W., "Spinodal decomposition in Al/Zn alloys", Journal of Materials Science, 4, 121 (1978).
26. Wu, C. K. and Thomas, G., "Microstructure and properties of a Cu-Ni-Cr alloy", Metallurgical Transactions, 8A, 1911 (1977).

27. Chou, A., Datta, A., Meier, G. H. and Soffa, W. A., "Microstructure behaviour and mechanical hardening in a Cu-Ni-Sn alloy", *Journal of Materials Science*, 13, 541 (1978).
28. Gregg, J. and Soffa, W. A., "Preliminary observations of the flow and fracture of copper-titanium alloy single crystals containing coherent precipitates", *Scripta Metallurgica*, 12, 525 (1978).
29. Gregg, J. and Soffa, W. A., "The strengthening and plastic properties of copper titanium alloy single crystals", Proceeding of the 5th international conference on strength of metals and alloys, Aachen, 1979, Haasen P. ed., (Pergamon, Toronto, 1980), p. 651.
30. Wagner, R., "Hardening by modulated structures in Cu-Ti Alloys", Proceeding of the 5th international conference on strength of metals and alloys, Aachen, 1979, Haasen P. ed., (Pergamon, Toronto, 1980), p. 645.
31. Laughlin, D. E. and Cahn, J. W., "Spinodal decomposition in age hardening copper-titanium alloys", *Acta Metallurgica*, 23, 329 (1975).
32. Kratochvil, P. and Haasen, P., "A model for an anomaly in the age hardening of Cu-Ti single crystals", *Scripta Metallurgica*, 16, 197 (1982).
33. Datta, A. and Soffa, W. A., "The structure and properties of age hardened Cu-Ti alloys", *Acta Metallurgica*, 24, 987 (1976).
34. Kato, M. and Schwartz, L. H., "The temperature dependence of yield stress and work hardening in spinodally decomposed Cu-10Ni-6Sn alloy", *Materials Science and Engineering*, 41, 137 (1979).
35. Vilassakdanont, A. and Subramanian, K. N., "Effect of temperature on some of the mechanical properties of Cu-10Ni-6Sn spinodal alloy", *Phys. Stat. Sol.*, 98, 553 (1985).
36. Lee, T. C., Shekhar, S., Vilassakdanont, A and Subramanian, K. N., "Mechanical properties of Cu-10Ni-6Sn alloy", Phase Transformation in Solids, Materials Research Society Symposia Proceedings, Tsakalakos, T. ed., North-Holland Publisher (1984), p. 577.
37. Louzon, T. J., "Tensile property improvements of spinodal Cu-15Ni-8Sn by two-phase heat treatment", *Transactions of the ASME*, 104, 234 (1982).

38. Schwartz, L. H. and Pleves, J. T., "Spinodal decomposition in Cu-9Ni-6Sn - II. A critical examination of mechanical strength of the spinodal alloys", *Acta Metallurgica*, 22, 911 (1974).
39. Quin, M. P. and Schwartz, L. H., "Low cycle fatigue in spinodal Cu-10Ni-6Sn", *Materials Science and Engineering*, 46, 249 (1980).
40. Sinning, H. -R. and Haasen, P., "The fatigue behaviour of spinodally decomposed Cu-4Ti single crystals", *Scripta Metallurgica*, 15, 85 (1981).
41. Lefevre, B. G., D'Annessa, A. T. and Kalish, D., "Age hardening in Cu-15Ni-8Sn alloy", *Metallurgical Transactions*, 9A, 577 (1978).
42. Ditchek, B. and Schwartz, L. H., "Diffraction study of spinodal decomposition in Cu-10Ni-6Sn", *Acta Metallurgica*, 28, 807 (1980).
43. Mott, N. F., Imperfections in Nearly Perfect Crystals, Shockley, W., Hollomon, J. H., Maurer, R. and Seitz, F. eds., John Wiley & Sons, New York, NY, 1952, p.173.
44. Mori, T. and Kato, M., "Asymptotic form of activation energy for double-kink formation in a dislocation in a one-dimensional periodic field", *Philosophical Magazine A*, 43, 1315 (1981).
45. Ditchek, B., Ph. D. Thesis, Northwestern University, IL, 1977.
46. Brown, L. M. and Ham, R. K., Strengthening Methods in Crystals, Kelly, A. and Nicholson, R. B. eds., Halsted Press Division, John Wiley & Sons, New York, NY, 1971, p.9.
47. Kato, M., Mori, T. and Schwartz, L. H., "The energetics of dislocation motion in spinodally modulated structures", *Materials Science and Engineering*, 51, 25 (1981).
48. Imura, T., "Contributions of HVEM in-situ experiments to dislocation dynamics", *Electron Microscopy*, 4, 280 (1980).
49. Fujita, H., "In-situ deformation by high voltage electron microscopy", *Electron Microscopy 1978*, Vol. 3, Sturgess, J. M. ed., Ninth International Congress on Electron Microscopy, Toronto, p.355.

50. Martin, J. L. and Kubin, L. P., "Optimum conditions for straining experiments in HVEM", *Phys. Stat. Sol.* 56, 487 (1979).
51. Makin, M. J., "Electron displacement damage in copper and aluminium in high voltage electron microscope", *Philosophical Magazine*, 18, 637 (1968).
52. Tabata, T., Fujita, H., Yamamoto, S. and Cyoji, T., "The effect of specimen diameter on tensile behaviors of aluminum thin wires", *Journal of the Physical Society of Japan*, 40, 792 (1976).
53. Fujita, H., Kawasaki, Y. and Furubayashi, E., "Metallurgical investigations with a 500KV electron microscope", *Japanese Journal of Applied Physics*, 6, 214 (1967)
54. Neuhäuser, H., "Slip-line formation and collective dislocation motion", Dislocations in Solids, Nabarro, F. R. N. ed., North-Holland Publishing Company, Vol. 6, 1983, p.321.
55. Fujita, H. and Yamada, H., "Multiplication of dislocations in aluminum", *Journal of the Physical Society of Japan*, 29, 132 (1970).
56. Shekhar, S., Ph. D. Thesis, Michigan State University, MI, 1985.
57. Kleintges, M., "Multiplication of dislocations in copper 0.6at% aluminum single crystals", *Scripta Metallurgica*, 14, 993 (1980).
58. Kleintges, M. and Haasen, P., "Revised measurements of dislocation velocities in Cu-Al single crystals", *Scripta Metallurgica*, 14, 999 (1980).
59. Neuhäuser, H., Koropp, J. and Heege, R., "Electron microscopic studies in the yield region of 70/30- $\alpha$ -brass single crystals - I. The mode of slip", *Acta Metallurgica*, 23, 441 (1975).
60. Honeycombe, R. W. K., The Plastic Deformation of Metals, Edward Arnold (Publishers) Limited, London, 1984, p.52.
61. Vesely, D., "In-situ deformation of molybdenum thin foils", *Journal of Microscopy*, 97, 191 (1973).
62. Vesely, D., "The study of deformation of thin foils of Mo under the electron microscope", *Phys. Stat. Sol.*, 29, 675 (1968).

63. Clement, N., Caillard, D. and Martin, J. L., "In-situ study of collective dislocation movements in a Ni-Cr alloy", Ninth International Congress on Electron Microscopy, 1, 568 (1978).
64. Clement, N., Monchoux, F. and Martin, J. L., "Estimation of friction forces in a concentrated face centered cubic Ni-Cr alloy", Proceeding of the 5th international conference on strength of metals and alloys, Aachen, 1979, Haasen P. ed., (Pergamon, Toronto, 1980), p. 1299.
65. Clement, N., Caillard, D. and Martin, J. L., "Heterogeneous deformation of concentrated Ni-Cr FCC alloys: Macroscopic and microscopic behaviour", Acta Metallurgica, 32, 961 (1984).